



trial origin of amino acids in carbonaceous meteorites. The remaining questions are whether amino acids can form in the interstellar medium (ISM) where new stars and planets are born, see [Glavin et al. 2020a](#) for a review), and how chiral symmetry of chiral molecules could be broken in the star- and planet-forming regions.

Complex organic molecules (COMs, e.g.,  $\text{CH}_3\text{OH}$  and  $\text{C}_2\text{H}_5\text{OH}$ ), the building blocks of amino acids and sugars, are believed to form in the ice mantle of interstellar dust grains from simple molecules such as  $\text{H}_2\text{O}$ ,  $\text{CO}$ ,  $\text{HCN}$ , and  $\text{NH}_3$  ([Herbst & van Dishoeck 2009](#); [Caselli & Ceccarelli 2012](#)). Independent experiments by [Bernstein et al. \(2002\)](#) and [Caro et al. \(2002\)](#) demonstrated that amino acids (including glycine, alanine, and serine) could be formed from irradiation of UV photons on the analogs of interstellar ice (consisting of water ( $\text{H}_2\text{O}$ ), hydrogen cyanide ( $\text{HCN}$ ), ammonia ( $\text{NH}_3$ ), methanol ( $\text{CH}_3\text{OH}$ )) (see also [Elsila et al. 2007](#)). UV irradiation on interstellar ice analogs can also form sugars [Meinert et al. \(2016\)](#). The recent experiment in [Ioppolo et al. \(2021\)](#) showed that glycine could be formed in the ice mantle without the need for energetic irradiation of UV radiation and CRs. [Parker et al. \(2023\)](#) suggested the concentration of amino acids in the Ryugu asteroid could arise from the formation of amino acids in the interstellar icy grains or ice mantle of grains in the presolar nebula, which then is accreted onto planetesimals during planet formation. Therefore, one plausible route is that amino acids are formed in the ice mantle of interstellar grains via UV photochemistry rather than formation in liquid water on an early Solar System body ([Elsila et al. 2007](#); [Oba et al. 2016](#); [Modica et al. 2018](#); [Oba et al. 2023](#); [Potiszil et al. 2023](#)).

In astrophysical environments, the first interstellar amino acid (propylene oxide) was discovered toward the Galactic center by [McGuire et al. \(2016\)](#) using the rotational spectroscopy observed with single-dish radio Green Bank Telescope (GBT). Recently, ethanolamine (a precursor of phospholipids, [Rivilla et al. 2022](#)) and glycine isomer ([Rivilla et al. 2023](#)) were detected toward the Galactic Center using the rotational spectroscopy using Yerkes 40 m and IRAM 30 m radio telescopes. These observations demonstrated that prebiotic chiral molecules could be formed in astrophysical environments.

UV circularly polarized light (UVCPL) is widely known to induce chiral asymmetry (i.e., enantiomer excess) due to selective destruction of one enantiomer of chiral molecules ([Flores et al. 1977](#); [Bonner 1991](#)). An experiment by [Modica et al. \(2014\)](#) showed that amino acids formed in ice mantles by irradiation of UVCPL on interstellar ice analogs have enantiomer excess. Circular

polarization of near-infrared light is observed in star-forming regions ([Bailey et al. 1998](#); [Kwon et al. 2016, 2018](#)). Therefore, the differential absorption of UVCPL by chiral molecules is a plausible mechanism producing the initial enantiomer excess and enantio-enrichment in the ISM ([Bailey 2001](#)). The limitation of this mechanism is that UVCPL cannot penetrate deep into dense clouds where new stars and planets are forming disks, and the enantiomer excess by UVCPL can be destroyed by other dynamical processes. To explain the chiral asymmetry of amino acids in meteorites/comets/asteroids, the enantiomer excess by UVCPL must be reserved during the planet formation process.

Very recently, a new promising channel to form COMs is introduced, through irradiation of low-energy electrons instead of UV photons. Numerous experiments [Boyer et al. \(2016\)](#); [Sullivan et al. \(2016\)](#); [Kipfer et al. \(2024\)](#) have demonstrated that irradiation of interstellar ice analogs with of low-energy electrons (energy below  $\sim 10 - 20$  eV) could trigger chemical reactions in similar ways as irradiation of UV photons. In particular, the experiment by [Esmaili et al. \(2018\)](#) showed that glycine can be formed by irradiation of low-energy electrons on interstellar analog of  $\text{CO}_2\text{-CH}_4\text{-NH}_3$  ice (see [Arumainayagam et al. \(2019\)](#) for a recent review on the role of photochemistry vs. radiation chemistry).

On the other hand, recent experiments established the key role of low-energy ( $\lesssim 10$  eV) spin-polarized electrons (SPEs) and ferromagnetic surfaces in producing chiral asymmetry (see reviews by [Naaman et al. 2018](#); [Rosenberg 2019](#)).<sup>1</sup> For example, [Rosenberg et al. \(2008\)](#) first demonstrated experimentally that low-energy SPEs resulting from irradiation of UV radiation on a magnetic substrate ([Kisker et al. 1982](#)) can induce chiral-selective chemical reactions of chiral molecules (2-butanol) in an adsorbed adlayer due to the CISS effect. Later on, [Rosenberg et al. \(2015\)](#) found that SPEs produced by X-ray irradiation on a nonmagnetic gold surface that are transmitted through a chiral overlayer<sup>2</sup> could induce chiral-selective chemistry in an adsorbed adlayer, which is caused by the different quantum yields for the reaction of SPEs with two enantiomers (see [Rosenberg 2019](#) for a review). Using the chiral-induced selective spin

<sup>1</sup> Early studies suggested that the chiral asymmetry might arise through the preferential destruction of one enantiomer in a racemic mixture by SPEs produced in the  $\beta$  decay of radioactive nuclei in weak interactions ([Lee & Yang 1956](#); [Wu et al. 1957](#)). However, the induced chirality asymmetry was found to be rather weak ([Hegstrom et al. 1980](#); [Bonner 1991](#)).

<sup>2</sup> Here the chiral overlayer acts as a filter that favors photoelectrons with a preferred spin state, so transmitted photoelectrons become spin-polarized.

(CISS) paradigm (Ray et al. 1999; Naaman & Waldeck 2012), Ozturk & Sassellov (2022) suggested that SPEs induced by UV irradiation of magnetic deposits in the basin of an evaporative lake might induce CISS-driven reduction chemistry (CDRC) for prebiotic molecules in the lake-magnetite basin interface, resulting in the chiral asymmetry. Experimental study in Ozturk et al. (2023a) showed that magnetic deposits act as chiral agents facilitating the homochiral enrichment of prebiotic compounds.

Hoang (2023) (Paper I) proposed that magnetically aligned dust grains play a key role in chiral asymmetry breaking for chiral molecules in astrophysical environments. First, aligned grains are a new source of SPEs due to the photoemission of electrons having aligned spins by the Barnett effect. Second, aligned grains induce chiral-dependent adsorption/crystalization of chiral molecules that would lead to chiral asymmetry of accumulated chiral molecules on aligned grains. They quantified the emission of SPEs from aligned grains due to the photoelectric effect of interstellar UV radiation. However, in dense molecular clouds and protostellar cores and disks, interstellar UV radiation is significantly attenuated. The dominant source of UV radiation is cosmic rays (CRs) because they can penetrate deep into dense regions. In particular, ice mantles of grains in dense clouds play a crucial role in astrochemistry, and COMs are thought to form in the grain ice mantle due to radical-radical reactions (Herbst & van Dishoeck 2009). Polarization observations toward star-forming regions reveal that icy grains are efficiently aligned (Whittet et al. 2008; Vaillancourt et al. 2020). Moreover, irradiation of CR electrons and protons on aligned grains would also cause the emission of spin-polarized secondary electrons. Note that previous experiments demonstrated that irradiation of energetic electrons (Unguris et al. 1982) and ions (Pfandzelter et al. 2003) on ferromagnetic grains can produce SPE as when irradiated by UV/X-ray photons (Kisker et al. 1982).

In this paper (Paper II), we explore the effect of CRs on the production of SPEs from aligned icy grains and their effect on chiral asymmetry of amino acids in dense protostellar environments where the UV interstellar radiation is substantially attenuated by high dust extinction. We focus on protostellar environments because these are the regions of active chemistry where most of COMs are detected. We study two important effects induced by CRs, including (1) photoemission of SPEs from aligned grains caused by UV radiation produced by the interaction of CRs and the gas, and (2) production of secondary SPEs by CRs bombardment onto aligned grains.

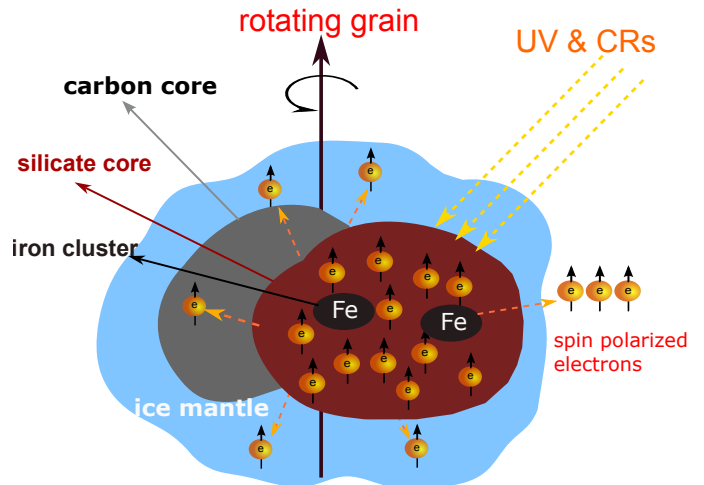


**Figure 1.** Schematic illustration of a model of icy grains in dense regions, including a grain core made of carbon and silicate core covered by an ice mantle. The silicate core contains embedded iron clusters. Irradiation of CRs and CR-induced UV radiation on the aligned rotating grain will produce spin-up or right-handed electrons.

The paper structure is described as follows. In Section 2, we study the magnetic alignment of icy grains using the leading theory of grain alignment. In Section 3 we study the effects of CRs on the  $H_2$  ionization and resulting UV radiation. In Section 4 we study the emission of SPEs by CR-induced UV radiation due to CR bombardment, and Section 5 is intended for discussion of the production of SPEs within aligned grains. Discussion and summary are shown in Sections 6 and 7, respectively.

## 2. MAGNETIC ALIGNMENT OF ICY GRAINS BY RADIATIVE TORQUES IN PROTOSTELLAR CORES

Here we briefly describe the key elements of the leading theory for magnetic alignment of grains with magnetic fields based on radiative torques and derive the minimum size of aligned grains in dense regions. For a detailed discussion on grain alignment physics, please refer to our latest papers (Hoang et al. 2021; Hoang 2022).

### 2.1. Magnetic properties and Larmor precession of icy dust grains

Magnetic properties of grains are essential for grain alignment with the magnetic field (Lazarian & Hoang 2007; Hoang & Lazarian 2016a; Lazarian & Hoang 2021). To describe the magnetic properties of dust in dense regions, we first assume a feasible dust model for these environments, which includes a grain core equivalent to the AstroDust model suggested by Hensley & Draine (2021)

for the diffuse ISM and an ice mantle as expected in dense and cold regions (Greenberg & Li 1998). In the Astro dust model, the composite grain consists of a silicate core containing embedded iron clusters and a carbon core (see Figure 1). The volume of our icy grain model is the sum of the volumes of the silicate core ( $V_{\text{Sil}}$ ), carbon core ( $V_{\text{carb}}$ ), and ice mantle ( $V_{\text{ice}}$ ):

$$\begin{aligned} V_{\text{grain}} &= V_{\text{Sil}} + V_{\text{carb}} + V_{\text{ice}} \\ &= V_{\text{Sil}} [1 + (V_{\text{carb}}/V_{\text{Sil}} + (V_{\text{ice}}/V_{\text{Sil}}))], \end{aligned} \quad (1)$$

where  $V_{\text{carb}}/V_{\text{Sil}} \approx 0.36$  for the Astro dust model (Hensley & Draine 2021). The volume of the ice mantle is uncertain, but typically the mantle has a thickness of  $L_{\text{ice}} \sim 100 \text{ \AA}$  (Greenberg & Li 1998). The effective radius of the icy grain is then  $a = (3V_{\text{grain}}/4\pi)^{1/3}$ .

Silicate grains are assumed to contain embedded iron clusters as a result of grain coagulation in dense clouds, and thus a superparamagnetic material. Therefore, the magnetic susceptibility of the silicate core is given by

$$\chi_{\text{sil,SPM}}(0) \approx 0.52 \left( \frac{N_{\text{cl}}}{100} \right) \left( \frac{\phi_{\text{sp}}}{0.1} \right) \left( \frac{p}{5.5} \right)^2 \left( \frac{10 \text{ K}}{T_{\text{d}}} \right), \quad (2)$$

where  $N_{\text{cl}}$  is the number of iron atoms per cluster,  $\phi_{\text{sp}}$  is the volume filling factor of iron clusters within the silicate core, and  $p = \mu_{\text{at}}/\mu_B$  with  $\mu_{\text{at}}$  being the atomic magnetic moment and  $\mu_B = e\hbar/2m_e c$  Bohr magneton (see (Hoang & Lazarian 2016a,b)). Above,  $N_{\text{cl}}$  spans from  $\sim 20$  to  $10^5$ ,  $\phi_{\text{sp}} \sim 0.3$  if 100% of Fe abundance present in iron clusters.

For an icy grain rotating with angular velocity  $\Omega$ , the effective magnetic moment resulting from the Barnett effect (Barnett 1915) (see e.g., Hoang 2022) is

$$\boldsymbol{\mu}_{\text{Bar}} = - \frac{\bar{\chi}_{\text{grain}}(0) V_{\text{grain}} \boldsymbol{\Omega}}{|\gamma_e|}, \quad (3)$$

where  $\bar{\chi}_{\text{grain}}(0)$  is the effective susceptibility of the icy grain of the volume  $V_{\text{grain}}$ , and  $|\gamma_e| \approx 2\mu_B/\hbar$  with  $\mu_B = e\hbar/2m_e c$  is the Bohr magneton.

The total magnetic moment of the icy grain can be calculated as

$$\begin{aligned} \boldsymbol{\mu}_{\text{Bar}} &= \boldsymbol{\mu}_{\text{sil}} + \boldsymbol{\mu}_{\text{carb}} + \boldsymbol{\mu}_{\text{ice}}, \\ &- \frac{\Omega}{|\gamma_e|} (\chi_{\text{sil,SPM}}(0) V_{\text{sil}} + \chi_{\text{carb}}(0) V_{\text{carb}} + \chi_{\text{ice}} V_{\text{ice}}), \end{aligned} \quad (4)$$

where  $\boldsymbol{\mu}_j, \chi_j$  with  $j = \text{sil, carb, ice}$  are the Barnett moment produced by the volume of silicate, carbon and ice mantle of their respective susceptibility  $\chi_j$ .

The carbon core and water ice mantle can have a small paramagnetic susceptibility due to defect and hydrogen nuclear spins due to the lack of unpaired electrons (Purcell 1979). Here we set  $\chi_{\text{carb}} \sim \chi_{\text{ice}} \sim 0$  due to their

subdominance to the silicate core. Equating Eqs. 5 to 3, the effective magnetic susceptibility of icy grains is reduced by a factor of

$$\begin{aligned} \frac{\bar{\chi}_{\text{grain}}(0)}{\chi_{\text{sil,SPM}}(0)} &= \frac{V_{\text{sil}}}{V_{\text{grain}}}, \\ &= \frac{1}{1 + (V_{\text{carb}}/V_{\text{sil}}) + (V_{\text{ice}}/V_{\text{sil}})}. \end{aligned} \quad (6)$$

For the typical thickness of ice mantle  $L_{\text{ice}} \sim 100 \text{ \AA}$ ,  $V_{\text{ice}}/V_{\text{Sil}} \sim 0.4$ , so that the effective magnetic susceptibility is reduced by a small factor of  $\bar{\chi}_{\text{grain}}/\chi_{\text{sil,SPM}} \sim 1/1.75 \approx 0.57$  for the silicate core with a typical radius of  $R_{\text{Sil}} = 0.1 \mu\text{m}$ . Therefore, the existence of thin ice mantles on the grain core does not significantly reduce the magnetic susceptibility of the superparamagnetic grain core. In realistic situations, Fe atoms from the gas phase can stick to the ice mantle, leading to Fe impurity and paramagnetic property of the ice mantle. This picture is supported by observations showing the gradual of Fe abundance in the gas phase from the diffuse ISM to MC (Savage & Bohlin 1979; Zhukovska et al. 2008; Jenkins 2009). Indeed, Sorrell (1994) suggested that Fe impurity, even of only 1% of Fe abundance in the ice mantle, can be transformed into iron oxide ( $\text{Fe}_3\text{O}_4$ ) due to heating by grain-grain collisions. Moreover, the bombardment of low-energy CRs can create a track in the ice and facilitate the aggregation of  $\text{Fe}_3\text{O}_4$  molecules into a cluster. This mechanism will form superparamagnetic magnetite clusters and make the ice mantle become superparamagnetic material. This is a promising process for enhancing the magnetic susceptibility of ice grains in dense regions.

The interaction of the grain magnetic moment (Eq. 3) with the external magnetic field causes the regular (Larmor) precession of the grain angular momentum around the magnetic field direction. The characteristic timescale of such a Larmor precession is given by

$$\begin{aligned} \tau_{\text{Lar}} &= \frac{2\pi I \Omega}{|\boldsymbol{\mu}_{\text{Bar}}| B} = \frac{2\pi |\gamma_e| I_{\parallel}}{\bar{\chi}_{\text{grain}}(0) V_{\text{grain}} B}, \\ &\simeq 8.4 \times 10^{-4} \hat{\rho} a_{-5}^2 \left( \frac{0.1}{\bar{\chi}_{\text{grain}}} \right) \left( \frac{5 \mu\text{G}}{B} \right) \text{ yr}, \end{aligned} \quad (8)$$

where  $I = 8\pi\rho a^5/15$  is the grain inertia moment,  $\rho$  is the grain mass density and  $\hat{\rho} = \rho/3 \text{ g cm}^{-3}$ , and  $B$  is the magnetic field strength of the cloud (Hoang 2022). The Larmor precession of grains with embedded iron clusters is much faster than the randomization of grain orientations by gas random collisions in protostellar environments (Hoang et al. 2021; Hoang 2022), so that the magnetic field is the axis of grain alignment.

## 2.2. Grain alignment with magnetic fields by radiative torques

Magnetic dust grains can align with the ambient magnetic field due to different physical processes, including the internal alignment of the grain axis of maximum inertia (e.g., short axis) with the angular momentum and the external alignment of the grain angular momentum with B-fields (Lazarian 2007; Lazarian et al. 2015; Hoang et al. 2022). The internal alignment is caused by Barnett and inelastic relaxation (Purcell 1979), which is found to be efficient for grains with embedded iron inclusions (Hoang et al. 2021; Hoang 2022). The external alignment is governed by radiative torques (Lazarian & Hoang 2007) and enhanced paramagnetic relaxation by magnetically enhanced radiative torque (MRAT) mechanism (Hoang & Lazarian 2008, 2016a).

Numerical simulations in Hoang & Lazarian (2008, 2016a) show that if the RAT alignment has a high-J attractor point, then, large grains can be perfectly aligned because grains at low-J attractors would be randomized by gas collisions and eventually transported to more stable high-J attractors by RATs. On the other hand, grain shapes with low-J attractors would have negligible alignment due to gas randomization. For small grains, numerical simulations show that the alignment degree is rather small even in the presence of iron inclusions because grains rotate subthermally (Hoang & Lazarian 2016a). Therefore, the degree of grain alignment depends critically on the critical size above which grains can be aligned by RATs, denoted by  $a_{\text{align}}$ .

Using the RAT paradigm, the minimum size of grain alignment depends on the local conditions of the gas and radiation field. For the dense core without embedded stars, grains are aligned by attenuated diffuse interstellar radiation field (ISRF). Following Hoang et al. (2021), the alignment size increases with the visual extinction  $A_V$  measured from the cloud surface inward as

$$a_{\text{align}} \simeq 0.11 \hat{\rho}^{-1/7} \left( \frac{\gamma_{-1} U_0}{n_4 T_{0,1}} \right)^{-2/7} \left( \frac{\bar{\lambda}_0}{1.2 \mu\text{m}} \right)^{4/7} \times (1 + 0.42 A_V^{1.22})^{(2-2/(4+\beta))/7} \times (1 + 0.27 A_V^{0.76})^{4/7} \mu\text{m}, \quad (9)$$

where  $n_4 = n_{\text{H}}/(10^4 \text{ cm}^{-3})$  is the normalized nucleon density,  $\bar{\lambda}_0$  and  $\gamma = 0.1\gamma_{-1}$  are the mean wavelength and anisotropy degree of the ISRF,  $T_{0,1} = T_0/10 \text{ K}$  with  $T_0 \sim 15 \text{ K}$  is the dust temperature at the surface of the cloud irradiated by the ISRF of strength  $U_0 = u_{\text{ISRF}}/u_{\text{MMP}} \sim 1$  with  $u_{\text{MMP}} = 8.64 \times 10^{-13} \text{ erg cm}^{-3}$  the energy density of the ISRF in the solar neighborhood from Mathis et al. (1983), and  $\beta \sim 1.5$  is the dust spectral index in dense cores.

**Table 1.** The minimum size of grain alignment by RATs in a starless core

| Parameters                        | Outer                | Inner                | Center          |
|-----------------------------------|----------------------|----------------------|-----------------|
| $N_{\text{H}_2} [\text{cm}^{-2}]$ | $3.2 \times 10^{21}$ | $2.8 \times 10^{22}$ | $10^{23}$       |
| $n_{\text{H}_2} [\text{cm}^{-3}]$ | $10^4$               | $10^6$               | $2 \times 10^7$ |
| $A_V [\text{mag}]$                | 1                    | 11                   | 39              |
| $a_{\text{align}} (\mu\text{m})$  | 0.12                 | 0.99                 | 4.9             |

Using the above equation, we can estimate the alignment size for three typical locations of the dense core (outer, inner, and central) considered in Ivlev et al. (2015), with the typical densities of  $[n_{\text{H}_2}, N_{\text{H}_2}] = [10^4 \text{ cm}^{-3}, 3.2 \times 10^{21} \text{ cm}^{-2}, [10^6 \text{ cm}^{-3}, 2.8 \times 10^{22} \text{ cm}^{-2}], [2 \times 10^7 \text{ cm}^{-3}, 10^{23} \text{ cm}^{-2}]$ . The corresponding values of visual extinctions are calculated using the typical formula  $A_V = (N_{\text{H}_2}/5.1 \times 10^{21} \text{ cm}^2) \times (3.1/R_V)$ , which yields  $A_V = [1, 11, 39]$ . The alignment size at these three locations are calculated using Equation 9. The results are shown in Table 1. One can see that large grains of size  $a \gtrsim 1 \mu\text{m}$  are still well aligned up to the inner region of the core. However, only very large grains of  $a > 5 \mu\text{m}$  can be aligned at the central region of the core due to the significant attenuation of the ISRF and the increase in the gas density (see Hoang et al. 2021 for more details).

In the presence of an embedded protostar, grain alignment can be driven by attenuated protostellar radiation. Consider a protostellar core with the density profile  $n_{\text{H}} = n_c \sim 10^7 - 10^8 \text{ cm}^{-3}$  for  $r < r_c$  and  $n_{\text{H}} = n_c (r/r_c)^{-p}$  with  $p \sim 1.5 - 2$  for  $r > r_c$  where  $r_c$  is the radius of the central region of  $\sim 30 \text{ au}$  for low-mass and  $r_c \sim 500 \text{ au}$  for high-mass protostars. Let  $L_\star$  and  $T_\star$  be the bolometric luminosity and effective temperature of the protostar. The typical visual extinction of the central region is  $A_V^*(r_c) \sim 30$  for low-mass protostars and  $A_V^*(r_c) \sim 50$  for high-mass protostars (see Hoang et al. 2021). Therefore, the UV protostellar radiation is significantly attenuated beyond a small region of  $A_V^* \sim 10$  around the protostar. Thus, the major volume of the protostellar core is dominantly irradiated by optical-NIR photons, with the mean wavelength of the protostellar radiation increasing rapidly with  $A_V^*$  (Hoang et al. 2021). The attenuated protostellar radiation, although has negligible effect on photoelectric effect, is essential for driving grain alignment by RATs. Following (Hoang et al. 2021), the alignment size at radius  $r$  and a visual extinction  $A_V^*$  measured from the

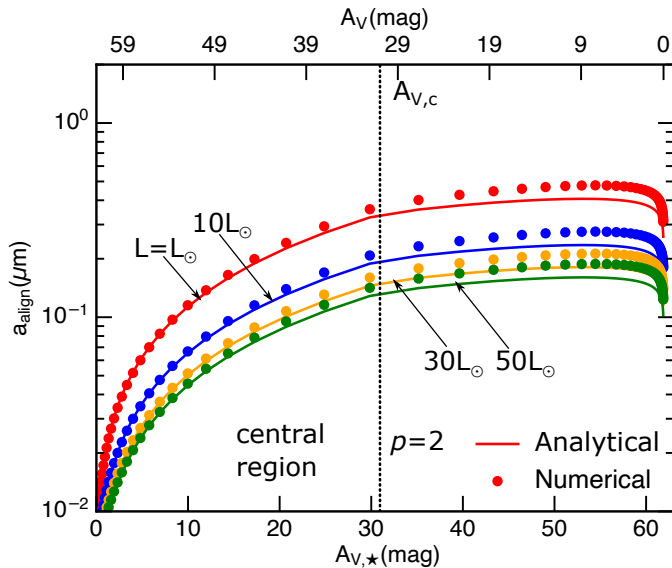


**Figure 2.** The minimum size of grain alignment by RATs in a protostellar core with the density profile with the slope of  $p = 2$  for the different luminosities. The vertical line marks the boundary between the central region and the envelope with  $A_{V,*} \sim 30$ . The alignment size increases with  $A_{V,*}$  due to attenuation of protostellar radiation. Results from Hoang et al. (2021).

protostar is estimated by

$$\begin{aligned}
 a_{\text{align}} \simeq & 0.031 \hat{\rho}^{-1/7} \left( \frac{U_{c,6}}{n_{c,8} T_{\text{in},2}} \right)^{-2/7} \left( \frac{\bar{\lambda}_*}{1.2 \mu\text{m}} \right)^{4/7} \\
 & \times (1 + c_1 A_{V,*}^{c_2})^{(2-q)/7} (1 + c_3 A_{V,*}^{c_4})^{4/7} \\
 & \times \left( \frac{r}{r_c} \right)^{2(2-p-q)/7} (1 + F_{\text{IR}})^{2/7} \mu\text{m}, \quad (10)
 \end{aligned}$$

where  $F_{\text{IR}}$  is the dimensionless parameter for describing the rotational damping by infrared dust emission,  $U_{c,6} = U_c/10^6$  where  $U_c = u_{\text{rad},c}/u_{\text{MMP}}$  with  $u_{\text{rad},c} = L_*/4\pi r_c^2 c$ ,  $q = 2/(\beta + 4)$ , and  $c_1 - c_4$  are the fitting parameters for the attenuation of protostellar radiation field (see Table 2 in Hoang et al. 2021).

Figure 2 shows the alignment size  $a_{\text{align}}$  for the protostellar core with the embedded protostars of different luminosity. For the low-mass protostar of  $L_* = 1L_\odot$  and  $T_* = 3000$  K, small grains larger than  $a > a_{\text{align}} \sim 0.1 \mu\text{m}$  can be aligned by protostellar radiation at the central region of  $A_{V,*} < 30$ , but only large grains of  $a \sim 0.5 \mu\text{m}$  can be aligned in the outer regions of  $A_{V,*} \sim 50 - 60$ . For a high-mass protostar of  $L_* \sim 10^3 L_\odot$  and  $T_* = 10^4$  K, the alignment sizes are smaller (see Table 1; for more details see Fig. 8 of Hoang et al. 2021). Note that observations reveal significant grain growth in dense protostellar environments and very large grains of size  $a > 10 \mu\text{m}$  can be present (see (Kwon et al. 2009;

Miotello et al. 2014; Galametz et al. 2019)). Therefore, large grains of  $a \gtrsim 0.1 \mu\text{m}$  in the protostellar cores can be magnetically aligned by RATs, as numerically demonstrated in (Giang et al. 2023).

### 3. COSMIC RAYS AND AND COSMIC RAYS-INDUCED UV RADIATION IN PROTOSTELLAR CORES

#### 3.1. Cosmic Ray Transport and CR Spectrum

Cosmic rays can penetrate into dense regions of the ISM and are expected to play an important role in producing SPEs in protostellar cores. CRs can produce SPEs either directly in collisions with aligned grains (by collisional ionization) or indirectly via the photoelectric effect by CR-induced UV radiation. To estimate the production rate of SPEs in protostellar cores, we need to know first the interstellar spectra of Galactic CRs and then perform the modeling of CRs transport in the dense regions to obtain attenuated CRs spectra.

The interstellar spectra of CRs, are actually not very well known, especially in the low-energy ( $\lesssim 1$  MeV) range which, as we shall see later, is particularly relevant for SPE production. This is partially due to the fact that the main sources of Galactic CRs are not yet unambiguously identified. Many different classes of sources have been proposed for high-energy CRs (from GeV to PeV), e.g. supernova remnants (SNRs, see e.g. Gabici et al. 2019; Cristofari 2021 for critical reviews), superbubbles (Parizot et al. 2004; Vieu et al. 2022), or star cluster (Morlino et al. 2021). Recently, progress on low-energy CRs has also been made thanks to the availability of data from Voyager probes and measurements of CR ionization rates<sup>3</sup> via molecular line observations. Some new classes of sources for MeV CRs have also been put forward in the literature for example, HII regions (Meng et al. 2019; Padovani et al. 2019), protostellar jets (Padovani et al. 2015, 2016; Gaches & Offner 2018), or wind termination shocks of stars (Scherer et al. 2008). Interestingly, enhanced CR ionization rates have been observed around several SNRs (Vaupré et al. 2014; Gabici & Montmerle 2015; Phan et al. 2020) which strongly indicate that these objects can be responsible for the entire Galactic CR spectra from MeV to PeV and maybe beyond. The expected interstellar spectra of CRs from SNRs match quite well with local observations of the CR spectra (see e.g. Phan et al. 2021).

For the sake of convenience and also account for the uncertainty in observed CR spectra, we adopt a para-

<sup>3</sup> Here, the CR ionization rate is defined as the production rate of  $\text{H}_2^+$  ions per  $\text{H}_2$  molecules (see e.g. Neufeld & Wolfire 2017).

metric model for the Galactic CR spectra as in Ivlev et al. (2015), which is described by

$$j_s(E) = C \frac{E^\alpha}{(E + E_0)^\beta} \text{ eV}^{-1} \text{ cm}^{-2} \text{ s}^{-1} \text{ sr}^{-1}, \quad (11)$$

where  $s = e, p$  denotes the CR electrons and protons,  $\alpha$  and  $\beta$  are the model parameters, and  $E_0 = 500$  MeV is the turnover energy of CR spectrum, and  $C$  is the normalization constant. For CR electrons,  $\alpha = \beta =$ , and  $C = 2.4 \times 10^{18}$ . For CR protons, we consider two models, model L (low) and model H (high), which have the parameters  $\alpha = 0.1, \beta = 2.8$  and  $\alpha = -1.5, \beta = 1.7$ , and  $C = 2.4 \times 10^{15}$ . We assume the lower cutoff of the spectrum to  $E_{\text{cut}} = 1$  keV and upper cutoff of  $E_{\text{max}} = 10$  GeV.

The Galactic CRs undergo energy loss due to interaction with the gas when penetrating into the dense core. This results in the attenuation of CRs with increasing the depth into the cloud or the column density  $N_{\text{H}_2}$ . To calculate the attenuated CR spectrum in the protostellar core at the column density  $N \equiv N_{\text{H}_2}$ , we follow the continuous slowing down approximation (CDSA) model (see Padovani et al. 2009), which yields

$$j_k(E, N) = j_k(E_0) \frac{L_k(E_0)}{L_k(E)}, \quad (12)$$

where  $k = e, p$ ,  $E_0$  is the initial energy and  $E$  is the energy of CRs that has passed a column density  $N_H$ ,  $L_k(E_0)$  and  $L_k(E)$  are the energy loss function at  $E_0$  and  $E$  respectively.

A detailed description of the CDSA model and numerical calculations are shown in Appendix C. In Figure 3, we only show the final results of the spectra of attenuated CR electrons and protons for the different column densities. The flux of low-energy CRs of energy below 1 MeV is significantly decreased with increasing  $N_{\text{H}_2}$  due to the ionization and electronic excitations of  $\text{H}_2$ . The high-energy CRs of  $E > 100$  MeV are hardly attenuated.

### 3.2. CR ionization rate per $\text{H}_2$

The total CR ionization rate per  $\text{H}_2$  can be calculated as (see Padovani et al. 2009)

$$\begin{aligned} \zeta(\text{H}_2) &= \int_{I(\text{H}_2)}^{E_{\text{max}}} (1 + \phi(E)) \sigma_{\text{H}_2}^{\text{CRe}}(E) 4\pi j_{\text{CRe}} dE \\ &+ \int_{I(\text{H}_2)}^{E_{\text{max}}} (1 + \phi(E)) \sigma_{\text{H}_2}^{\text{CRp}}(E) 4\pi j_{\text{CRp}} dE \\ &+ \int_0^{E_{\text{max}}} \sigma_{\text{H}_2}^{\text{CRp,e.c}} j_{\text{CRp}} dE, \end{aligned} \quad (13)$$

where  $I(\text{H}_2) = 15.603$  eV,  $\phi(E)$  is the correction factor accounting for ionization of  $\text{H}_2$  by secondary electrons,

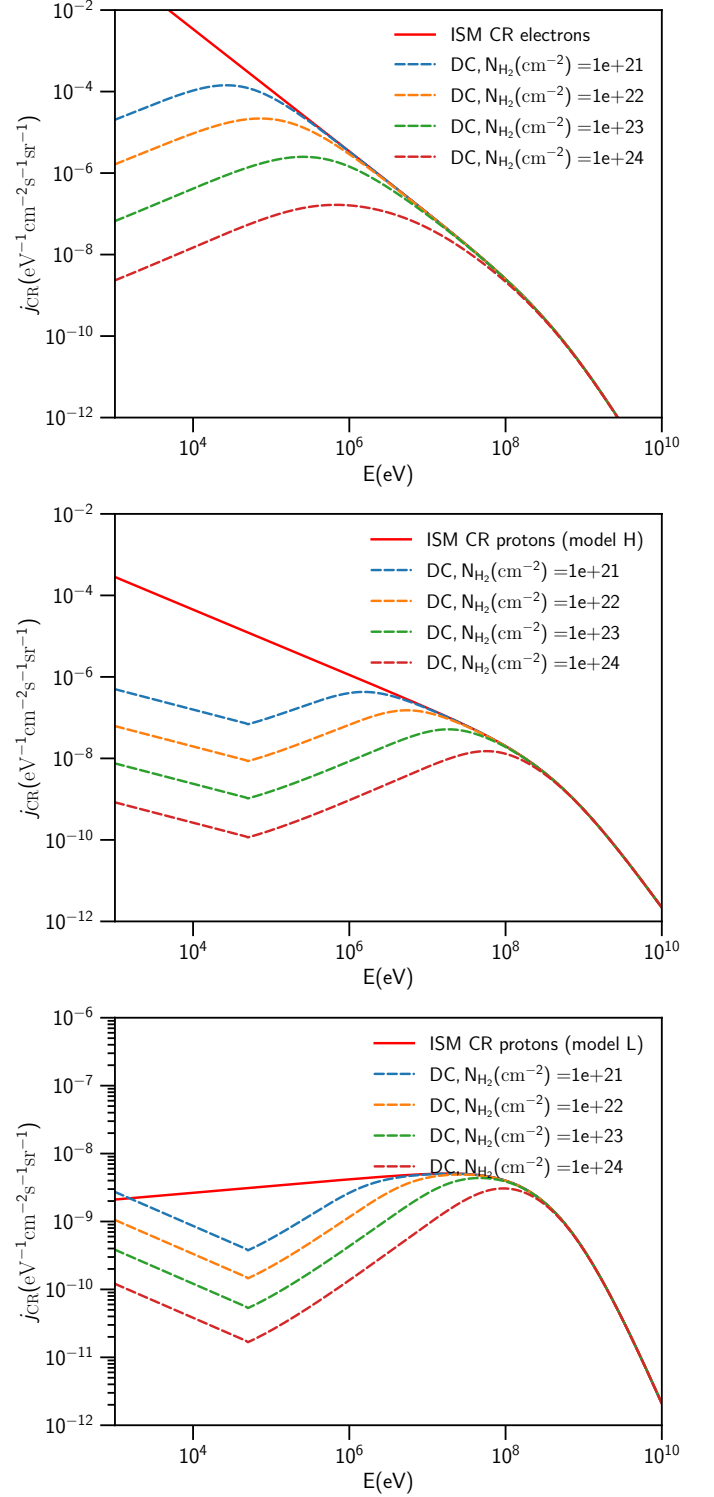


**Figure 3.** Spectra of CR electrons (top panel) and CR protons (middle and bottom panels for model H and L) at the diffuse ISM (solid lines) and estimated in dense clouds (DC) with different column densities  $N_{\text{H}_2}$  using the continuous slowing down approximation model.

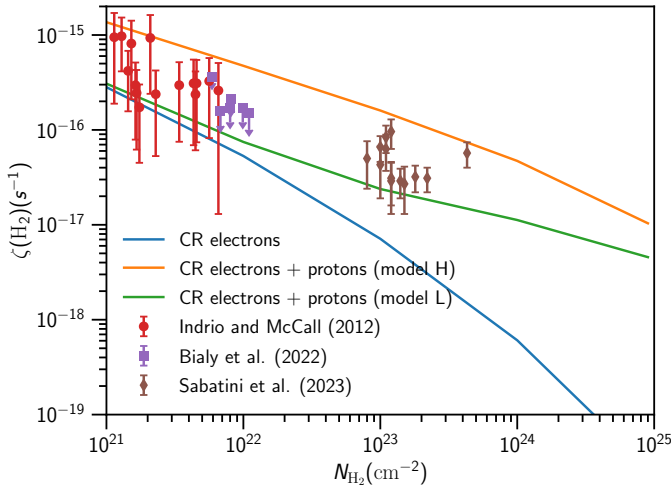


**Figure 4.** Cosmic-ray ionization rates calculated for the different column densities and comparison to observational data from Indriolo & McCall (2012) and Sabatini et al. (2023), and upper limits from Bialy et al. (2022). The L and H models constitute the lower and upper bounds for the observations above  $3 \times 10^{21} \text{ cm}^{-2}$ .

$\sigma^{\text{CRe}}, \sigma^{\text{CRp}}$  are the ionization cross-sections of  $\text{H}_2$  by CRe and CRp, and  $\sigma^{\text{CRp,ec}}$  is the cross-section for CR proton capture by  $\text{H}_2$  via the process  $p + \text{H}_2 \rightarrow \text{H} + \text{H}_2^+$  (see Appendix A).

Using the attenuated CR spectra from Figure 3, we calculate  $\zeta(\text{H}_2)$  by both CR electrons and protons. Results are shown in Figure 4 as a function of the column density  $N_{\text{H}_2}$  (solid line). Measurements from various observations of dense clouds and protostellar cores (Caselli et al. 1998; Indriolo & McCall 2012; Redaelli et al. 2021; Bialy et al. 2022; Sabatini et al. 2023) are overplotted for comparison. The data show strong scatters in the diffuse region of  $N_{\text{H}_2} < 3 \times 10^{21} \text{ cm}^{-2}$ , but can be well constrained by the model L and model H for dense regions of  $N_{\text{H}_2} > 3 \times 10^{21} \text{ cm}^{-2}$ . The CR ionization tends to decrease with increasing the gas column density due to the CR energy loss.

### 3.3. UV radiation from $\text{H}_2$ fluorescence by cosmic rays

The interaction of CRs with interstellar gas can produce radiation via several mechanisms, including CR electron Bremsstrahlung,  $\text{H}_2$  fluorescence, and  $\pi^0$  decay (see e.g., Ivlev et al. 2015). The  $\text{H}_2$  fluorescence produces UV photons with energy around 11.2-13.6 eV due to CR-induced excitations of  $\text{H}_2$  molecules into the Lyman-Werner states (Ivlev et al. 2015), which is the most important process for the production of SPES via photoelectric effect.

The flux of CR-induced UV photon flux  $\Phi_{\text{UV}}$  can be approximately estimated for high-column-density clouds using the CR ionization rate  $\zeta(\text{H}_2)$  by (Padovani et al.

2024)

$$\Phi_{\text{UV}} \simeq 100(c_0 + c_1 R_V + c_2 R_V^2) \left( \frac{\zeta(\text{H}_2)}{10^{-17} \text{ s}^{-1}} \right) \text{ cm}^{-2} \text{ s}^{-1} \quad (14)$$

where  $[c_0, c_1, c_2] = [5.023, -0.504, 0.115]$ ,  $R_V$  is total-to-selective dust extinction. The above linear relation is only valid for  $3.1 \leq R_V \leq 5.5$  and in the dense regions with  $N_{\text{H}} \gtrsim 10^{22} \text{ cm}^{-2}$ .

Also, since CR-induced UV radiations are produced by secondary electrons from CR ionization events, a linear relation between  $\Phi_{\text{UV}}$  and  $\zeta(\text{H}_2)$  is expected. Using the spectra of attenuated CRs obtained in the previous section (Fig. 3), we can calculate  $\Phi_{\text{UV}}$  using Equation 14.

### 3.4. Thermal Electrons produced by CR ionization of $\text{H}_2$

In dense regions, the main source of gas ionization is by CRs and CR-induced UV radiation. The gas ionization fraction,  $x_e$ , can be described by (Ivlev et al. 2015)

$$x_e \simeq 1.7 \times 10^{-8} \left( \frac{n_{\text{H}_2}}{10^4 \text{ cm}^{-3}} \right)^{-0.65} \left( \frac{\zeta(\text{H}_2)}{10^{-17} \text{ s}^{-1}} \right)^{1/2} \quad (15)$$

which increases with the CR ionization rate and decreases with the gas volume density.

The number density of thermal electrons is then calculated by  $n_e = x_e n(\text{H}_2)$ , which yields the flux of thermal electrons

$$\begin{aligned} \Phi_{\text{Te}} &= x_e n_{\text{H}_2} v_{\text{Te}}, \\ &\simeq 3642 \left( \frac{n_{\text{H}_2}}{10^4 \text{ cm}^{-3}} \right)^{-0.35} \left( \frac{T_{\text{gas}}}{100 \text{ K}} \right)^{1/2} \\ &\times \left( \frac{\zeta(\text{H}_2)}{10^{-17} \text{ s}^{-1}} \right)^{1/2}. \end{aligned} \quad (16)$$

Compared to the flux of CR electrons, one can see that  $\Phi_{\text{Te}}$  is two orders of magnitude higher than the CR electron flux. However,  $\Phi_{\text{Te}}$  is slightly higher than the UV flux (see Eq. 14).

## 4. SPIN POLARIZATION AND EMISSION OF SPES FROM ALIGNED GRAINS

CR electrons and thermal electrons produced by  $\text{H}_2$  ionization by CRs are expected to have random spins, i.e., un-polarized. Here, we first show that the collection of thermal and CR electrons/protons onto aligned grains will quickly produce spin-polarization due to the Barnett effect. We then discuss the emission of SPES by CR-induced energetic radiation and CR electrons.



#### 4.1. Collection of thermal electrons and CR electrons

##### 4.1.1. Thermal electrons

Thermal electrons will be collected by the dust grain upon collisions. The collection rate of thermal electrons by a grain of size  $a$  is given by

$$\begin{aligned} J_{\text{coll,Te}} &= n_e v_{\text{Te}} \pi a^2 g(\phi_Z) \text{ s}^{-1}, \\ &\simeq 5 \times 10^{-7} a_{-5}^2 n_5^{-0.35} g(\phi_Z) \left( \frac{T_{\text{gas}}}{100 \text{ K}} \right)^{1/2} \\ &\times \left( \frac{\zeta(\text{H}_2)}{10^{-17} \text{ s}^{-1}} \right)^{1/2} \end{aligned} \quad (17)$$

where  $v_{\text{Te}} = (8kT_{\text{gas}}/(\pi m_e))^{1/2}$  is the thermal speed of electrons,  $g(\phi_Z)$  with  $\phi_Z = Z_{\text{grain}} e^2/a$  and  $Z_{\text{grain}}$  the grain charge. Here,  $g = e^{\phi_Z/kT_{\text{gas}}}$  for  $Z_{\text{grain}} < 0$  and  $g(\phi_Z) = 1 + \phi_Z/kT_{\text{gas}}$  for  $Z_{\text{grain}} \geq 0$  that accounts for the Coulomb effect on electron collision cross-section. Throughout this exploratory paper, we consider neutral grains of  $Z_{\text{grain}} = 0$  for convenience.

For the charge neutrality condition,  $n_e = n_i$ , the rate of electron collection is larger than that of protons due to larger electron velocity, which can be disregarded.

##### 4.1.2. Collection of CR Electrons

Grains may also capture CR electrons and protons upon CR bombardment. The collection rate of CR electrons by a grain of size  $a$  is given by [Draine & Salpeter \(1979\)](#)

$$J_{\text{coll,CRe}}(a, Z) = \pi a^2 \int_{E_{\text{int}}}^{\infty} 4\pi j_{\text{CRe}}(E) s_e(E) dE, \text{ s}^{-1} \quad (18)$$

where  $s_e$  is the sticking coefficient of CR electrons, and  $E_{\text{int}}$  is the minimum energy for the grain-CR interaction.

The sticking coefficient  $s_e(E)$  is equal 1 for the stopping range  $R_e(E) < 4a/3$  and  $s_e = 0$  for  $R_e(E) > 4a/3$  where

$$R_e(E) = (An)^{-1} E^n \simeq 0.03 \rho^{-0.85} (E/1 \text{ keV})^n \mu\text{m}, \quad (19)$$

where  $n = 1.5$  for electron energy from 300 eV to 1 MeV ([Draine & Salpeter 1979](#), see [Hoang et al. 2015](#)). One can see that for CR electrons of  $E > 100$  keV, the stopping range is  $R_e(E) > 30 \mu\text{m}$ . Therefore, for grains of  $a \sim 1 \mu\text{m}$  in protostellar environments, CR electrons do not stick to the grain but pass through, so one has  $s_e = 0$ . The same effect is expected for CR protons.

Since the flux of CR electrons and protons,  $j_{\text{CRe,CRp}}$ , is much lower than the flux of thermal electron density  $j_{\text{Te}}$  (see Eq. 16), the collection of CR electrons/protons is negligible compared to the collection of thermal electrons.

#### 4.2. Spin Polarization of Captured Electrons by the Barnett Effect

Electrons captured by a dust grain are most likely present in the outermost shell of atomic energy configuration and become unpaired electrons of the grain atoms. These unpaired electrons with initially random spins will be polarized due to the Barnett effects and have spins aligned along the grain rotation axis if the timescale for spin alignment is much shorter than the time interval between two CR electron bombardments. Let us estimate these timescales for dust grains.

The equivalent magnetic field induced by the Barnett effect for a rotating grain of angular velocity  $\Omega$  is given (e.g., [Hoang & Truong 2024](#))

$$\begin{aligned} B_{\text{Barnett}} &= \frac{\Omega}{|\gamma_e|} = \frac{2m_e c}{eg_e} \Omega, \\ &\simeq 3\rho^{-1/2} T_{g,1}^{1/2} s^{-1/2} a_{-5}^{-5/2} \left( \frac{\Omega}{\Omega_T} \right) \text{ mG}, \end{aligned} \quad (20)$$

where  $g_e \approx 2$  for electrons, and  $s$  is the parameter describing grain shape of the order of unity. For aligned grains of  $a > a_{\text{align}}$  by RATs, one has  $\Omega/\Omega_T \gtrsim 3$ . Thus, aligned grains would produce  $B_{\text{Barnett}} \gtrsim 1 \text{ mG}$ .

The Larmor precession timescale of the electron spin in this Barnett magnetic field is given by

$$\begin{aligned} \tau_{\text{Lar}} &= \frac{2\pi}{\omega_{\text{Lar}}} = \frac{2\pi S}{\mu_{el} B_{\text{Barnett}}} \quad (21) \\ &\simeq \frac{3.5\pi m_e c}{e B_{\text{Barnett}}} \simeq 6.2 \times 10^{-4} \frac{1 \text{ mG}}{B_{\text{Barnett}}} \text{ s}, \end{aligned} \quad (22)$$

where  $S = \sqrt{s_e(s_e + 1)} \hbar$  with  $s_e = 1/2$  for electrons.

For the flux of CR electrons of  $\Phi_{\text{CRe}} = n_{\text{CRe}} \bar{V}_{\text{CRe}}$  with  $\bar{V}_{\text{CRe}}$  the average speed of CR electrons, the time interval between two CRe bombardments is

$$\tau_{\text{CRe}} = \frac{1}{\pi a^2 n_{\text{CRe}} \bar{V}_{\text{CRe}}} \quad (23)$$

$$\simeq 33.6 a_{-5}^{-2} \left( \frac{10^{-8} \text{ cm}^{-3}}{n_{\text{CRe}}} \right) \left( \frac{0.1c}{v_{\text{CRe}}} \right) \text{ yr}. \quad (24)$$

The timescale of UV absorption that induces photoemission is given by

$$\tau_{\text{UV}} = \frac{1}{\pi a^2 \Phi_{\text{UV}}} \quad (25)$$

$$\simeq 0.3 a_{-5}^{-2} \left( \frac{10^{-17} \text{ s}^{-1}}{\zeta(\text{H}_2)} \right) \text{ yr}, \quad (26)$$

where  $\Phi_{\text{UV}}$  is given by Eq. 14.

Comparing Equations (24) and (26) to Equation 22, one can see that the spin alignment timescale by the Barnett effect is much shorter than the timescale of UV absorption and CR bombardment. Therefore, captured

electrons are quickly spin-polarized before the ejection by UV and CR bombardments. As a result, electrons ejected by UV/CR bombardment are spin-polarized.

### 4.3. Emission of Spin-Polarized Electrons

#### 4.3.1. Photoemission by CR-induced UV Radiation

Irradiation of dust grains aligned with the ambient magnetic field by unpolarized UV radiation would eject spin-polarized electrons with spins aligned along the magnetic field (Hoang 2023). The thermal electrons captured by the grain will be easiest to be ejected due to their loosen bound to the grain atoms. Here we study the emission of SPEs from aligned grains by CR-induced UV radiation.

Let  $Y(a, \nu)$  be the photoelectric yield of a grain of size  $a$  induced by a photon of frequency  $\nu$ . The rate of photoelectron emission of primary electrons from one grain (electrons per second) is

$$J_{\text{pe}}(a) = \int_{\nu_{\text{pet}}}^{\infty} Y(a, \nu) \pi a^2 Q_{\text{abs}} \frac{cu_{\nu}}{h\nu} d\nu, \quad (27)$$

$$\begin{aligned} &= \pi a^2 \Phi_{\text{UV}} \langle Y(a, \nu) Q_{\text{abs}} \rangle \\ &\simeq 10^{-8} a_{-5}^2 (c_0 + c_1 R_V + c_2 R_V^2) \left( \frac{\zeta(\text{H}_2)}{10^{-17} \text{ s}^{-1}} \right) \\ &\quad \times \langle Y(a, \nu) Q_{\text{abs}} \rangle, \end{aligned} \quad (28)$$

where  $Q_{\text{abs}}$  is the absorption efficiency,  $\nu_{\text{pet}}$  is the frequency threshold required for the photoelectric effect, which is determined by the ionization potential (IP), i.e.,  $h\nu_{\text{pet}} = \text{IP}$ , and  $u_{\nu}$  is the specific energy density of the radiation field. Here we take the ionization potential  $\text{IP} = W = 8 \text{ eV}$  for silicate grains (see Weingartner & Draine 2001). The energy density spectrum  $u_{\nu}$  is the UV radiation induced by CRs with the flux  $u_{\text{UV}} = \int u_{\nu} d\nu = \Phi_{\text{UV}}/c$  given by Equation (14), and  $\langle YQ_{\text{abs}} \rangle = \int YQ_{\text{abs}} cu_{\nu} d\nu / \Phi_{\text{UV}}$ .

For the CR-induced UV radiation of  $h\nu \sim 11.2 - 13.6 \text{ eV}$ , we adopt  $\langle YQ_{\text{abs}} \rangle = 0.1$  because  $Y \sim 0.1$  for aligned grains of  $1 \mu\text{m} > a > 0.1 \mu\text{m}$  and  $Q_{\text{abs}} \approx 1$  (Hoang et al. 2015; Hoang 2023).

Figure 5 shows the flux of CR-induced UV radiation (upper panel) and the rate of photoemission (lower panel) as functions of the column density. The effect of CR protons is more important in producing UV radiation and then photoemission than CR electrons.

#### 4.3.2. Secondary electron emission by CRs

Irradiation of dust grains by CR electrons and protons can create secondary electrons in the inner shell of atoms. Such energetic electrons can cause the ejection of electrons on the way to the grain surface, producing a higher abundance of electrons, an effect similar to

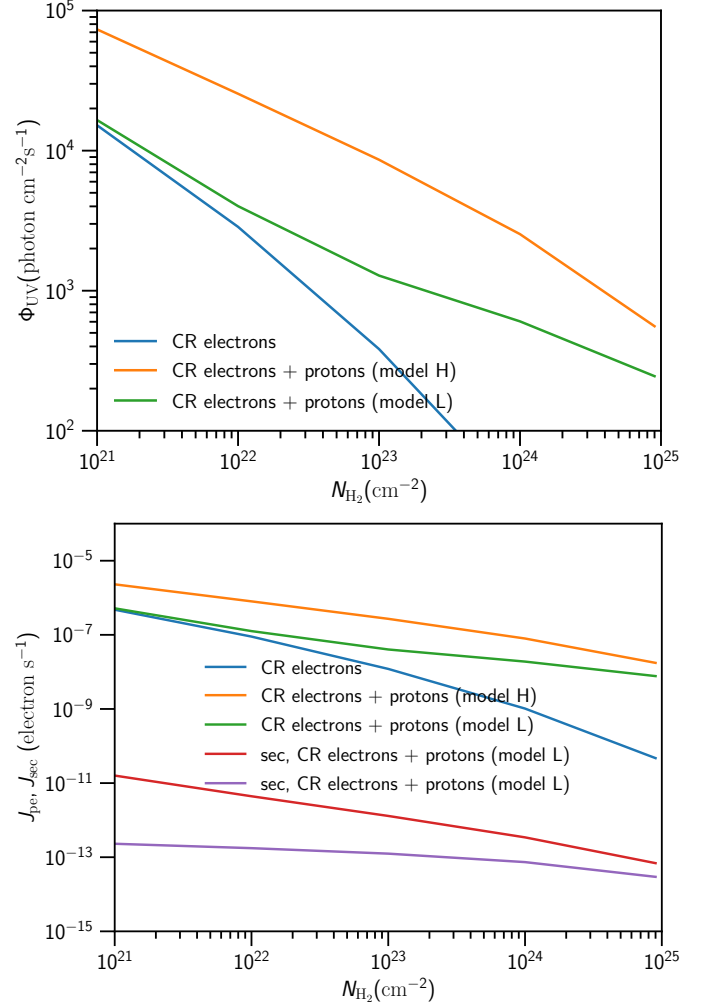


**Figure 5.** The emission rate of photoelectrons by CR-induced UV radiation and secondary electrons by CR bombardment. Photoemission is dominant over secondary electron emission. The grain size of  $a = 0.1 \mu\text{m}$  is adopted.

the Auger effect caused by X-rays (Hoang et al. 2015). The secondary electrons usually have low energy (Arumainayagam et al. 2010). These low-energy secondary electrons include mostly unpaired electrons because they have lower ionization potential.

The rate of secondary electron emission from the grain (electrons per second) by CRs is given by

$$J_{\text{sec},k}(a, Z) = \pi a^2 \int_{E_{\text{int}}}^{\infty} 4\pi j_k(E) \delta_e(E) dE, \quad (29)$$

where  $k = e, p$ ,  $\delta_e$  is the secondary photoelectric yield (Draine & Salpeter 1979), which can be approximately given by Hoang & Loeb (2017)

$$\delta_e(E) = 4\delta_e^{\text{max}} \left( \frac{E}{E_{\text{max}}} \right) \frac{1}{(1 + E/E_{\text{max}})^2}, \quad (30)$$

where  $\delta_e^{\max} \sim 1.5 - 2$ ,  $E_{\max} \sim 0.2 - 0.4$  keV (cf. Ivlev et al. 2015). The above equation implies that the secondary emission yield is  $\delta_e \sim \delta_{\max}$  at  $E = E_{\max}$ , and it decreases rapidly for  $E \gg E_{\max}$  as  $\delta_e/\delta_{\max} \sim 4(E/E_{\max})^{-1} \sim 0.012(E_{\max}/0.3\text{keV})(100\text{keV}/E)$ .

The rate of secondary electron emission by CR electrons and protons is shown in Figure 5 (lower panel). The secondary electron emission by CRs is negligible compared to photoemission by CR-induced UV radiation.

#### 4.3.3. Fraction of spin-polarized photoelectrons and secondary electrons

Photoelectrons and secondary electrons emitted by CR effects mostly arise from electrons in the outermost electronic shells (valence shell) that are the most loosely bound to the nucleus. Now, we estimate the fraction of SPEs among photoelectrons and secondary electrons.

First, for photoemission of unpaired thermal electrons collected by aligned grains, the fraction of SPEs among photoelectrons is  $f_{\text{SPE}} = 100\%$  because captured electrons are most likely unpaired because they are loosely bound to atoms on the outermost energy shell.

Second, if photoelectrons are emitted from the original dust grain, the fraction of SPEs can be estimated as

$$f_{\text{SPE}} = \frac{N_{\text{unpair}}}{N_{\text{valence}}}. \quad (31)$$

For the silicate core of the typical olivine structure  $\text{MgFeSiO}_4$ , the number of valence electrons is  $n_{\text{valence}} = 32$ , and the number of unpaired electrons is  $n_{\text{unpair}} = 4$ , which yields ratio of unpaired to valence electrons is  $f_{\text{SPE}} = 1/8$  per molecule.<sup>4</sup> For metallic iron with 8 electrons in the outermost shell ( $4s^23d^6$ ) and 4 unpaired electrons in  $3d^6$ , one has  $f_{\text{SPE}} = 4/8 = 1/2$  per iron atom. Table 2 shows the results for several typical silicate compositions.

For the silicate structure of  $\text{MgFeSiO}_4$  with embedded iron inclusions, let  $\phi_{\text{Fe}}$  be the volume filling factor of metallic iron. The volume of metallic iron is  $V_{\text{Fe}} = \phi_{\text{Fe}}V_{\text{grain}}$  and the volume of silicate is  $V_{\text{silicate}} = (1 - \phi_{\text{Fe}})V_{\text{grain}}$  where  $V_{\text{grain}} = 4\pi a^3/3$ .

<sup>4</sup> In the  $\text{MgFeSiO}_4$  molecule, the ionic bonds between  $\text{Fe}^{2+}\text{-O}^{2-}$  and  $\text{Mg}^{2+}\text{-O}^{2-}$ , and covalent bonds between Si-O. The number of valence electrons include 2 electrons from  $\text{Mg}^{2+}$ , 2 electrons from  $\text{Fe}^{2+}$ , 4 electrons from Si, and 6 electrons in the outermost shell ( $2s^22p^4$ ) from each O, which sums up to 32 valence electrons. Note that both Mg and Fe have two electrons in the outermost shell  $3s^2$  and  $4s^2$  so that they can donate 2 electrons for O to fill the orbital  $2p^4$ , making ionic bonds.

We have the total number of valence and unpaired electrons in the grain of size  $a$  are

$$N_{\text{valence}} = n_{\text{val}}(\text{Fe}) \frac{\phi_{\text{Fe}}V_{\text{grain}}}{v_{\text{Fe}}} + n_{\text{val}}(\text{Sil}) \frac{(1 - \phi_{\text{Fe}})V_{\text{grain}}}{v_{\text{Sil}}}, \quad (32)$$

$$N_{\text{unpair}} = n_{\text{unpair}}(\text{Fe}) \frac{\phi_{\text{Fe}}V_{\text{grain}}}{v_{\text{Fe}}} + n_{\text{unpair}}(\text{Sil}) \frac{(1 - \phi_{\text{Fe}})V_{\text{grain}}}{v_{\text{Sil}}}, \quad (33)$$

where  $v_{\text{Fe}} = 4\pi a_{\text{Fe}}^3/3 = 1.15 \times 10^{-23}$  cm with  $a_{\text{Fe}} \approx 1.4\text{\AA}$  is the Fe atom volume, and  $v_{\text{Sil}} = 3.5 \times 10^{-23}$  cm is the volume of the silicate molecule  $\text{MgFeSiO}_4$ .

Using Equation 31 one obtain  $f_{\text{SPE}} = 0.125$  for  $\phi_{\text{Fe}} = 0$  (i.e., only silicate) and  $f_{\text{SPE}} = 0.22$  for silicate with embedded iron clusters at the maximum Fe volume filling factor of  $\phi_{\text{Fe}} = 0.3$  (Hoang & Lazarian 2016a). Therefore, the fraction of SPEs is about 10% for silicate grains with embedded irons.

When the value of  $f_{\text{SPE}}$  is available in Table 2, one can calculate the total emission rate of SPEs from the aligned grain as

$$J_{\text{SPE}} = f_{\text{SPE}}(J_{\text{pe}} + J_{\text{sec}}), \quad (34)$$

where the second term is subdominant than the first term.

Using the photoemission rate shown in Figure 5 and the values of  $f_{\text{SPE}}$  in Table 2, one can estimate the photoemission rate of SPEs is  $J_{\text{SPE}} \sim 10^{-10} f_{\text{SPE}} \text{s}^{-1}$ . The flux of SPEs is then  $\Phi_{\text{SPE}}^{\text{em}} = J_{\text{SPE}}/(4\pi a^2) \sim 0.08 f_{\text{SPE}} a_{-5}^{-2} \text{cm}^{-2} \text{s}^{-1}$ .

## 5. PRODUCTION OF SECONDARY SPES WITHIN ALIGNED GRAINS BY CRs

Secondary SPEs produced within an aligned grain by CR bombardment play an important role for chemistry in the icy grain mantle. Here, we estimate the rate of secondary SPEs produced by CR electrons and protons.

### 5.1. Range of CR electrons and protons in dust

Above, we have studied the collection of electrons and emission of photoelectrons and secondary electrons from aligned grains. Because UV photons have attenuation length  $l_a \sim \lambda/(4\pi\text{Im}(m))$  with  $m$  the refractive index of the dust at wavelength  $\lambda$  with a typical value of  $l_a \approx 0.01 \mu\text{m}$  (Weingartner & Draine 2001), UV photons can cause photoemission of electrons from the surface layer of  $0.01 \mu\text{m}$  of the grain. However, CR electrons/protons have the range (see (Hoang et al. 2015))

$$R_e \simeq 0.01 \hat{\rho}^{-0.85} (E_e/1 \text{keV})^{1.5} \mu\text{m}, \quad (35)$$

$$R_p \simeq 0.01 \hat{\rho}^{-1} (E_p/1 \text{keV}) \mu\text{m}, \quad (36)$$

which can excite electrons deep inside the grain.

**Table 2.** Fraction of unpaired electrons to valence in popular molecules

| Molecules                                   | Valence Electrons, $n_{\text{val}}$ | Unpaired Electrons, $n_{\text{unpair}}$ | Fraction, $f_{\text{SPE}}$ |
|---|-------------------------------------|---|----------------------------|
| Olivine (MgFeSiO <sub>4</sub> )             | 2(Mg)+ 2(Fe)+ 4(Si)+24 (O4)= 32     | 4                                       | 1/8                        |
| Pyroxene (FeSiO <sub>3</sub> )              | 2(Fe)+ 4(Si) + 18 (O3)=24           | 4                                       | 1/6                        |
| Metallic Iron (Fe)                          | 8                                   | 4                                       | 1/2                        |
| Wüstite (FeO)                               | 2(Fe)+ 6 (O)=8                      | 4                                       | 1/2                        |
| Hematite (Fe <sub>2</sub> O <sub>3</sub> )  | 4(Fe2) + 18 (O3)=22                 | 10                                      | 5/11                       |
| Maghemite (Fe <sub>3</sub> O <sub>4</sub> ) | 6 (Fe3)+ 24 (O4)=30                 | 14                                      | 7/15                       |
| Carbon (C)                                  | 4                                   | 0                                       | 0                          |

We note that only the secondary electrons that have sufficient energy can travel from the grain core to the surface and be able to escape from the grain. The remaining secondary electrons cannot escape the grain, but they can still trigger chemical reactions of radical and simple molecules to form COMs and amino acids, leading to chiral asymmetry. Here, we first estimate the fraction of SPEs created inside an aligned grains by CR electrons and protons.

### 5.2. Flux of secondary SPEs produced by CR electrons and protons

Upon passing through the dust grains, CR electrons and protons lose their energy through various electronic processes including ionization and excitation (see Hoang et al. 2015 for details). The energy loss is given in Appendix B15.

Let  $w$  be the average energy required to create an electron-hole pair within the grain, which has the value of  $\sim 10-30\text{eV}$  for silicate. Assuming the effective spherical grain of size  $a$  as a slab of thickness  $4a/3$ , the rate of SPEs produced by an aligned grain within the protostellar core to that the CR traverses the hydrogen column density  $N = N_{\text{H}_2}$ :

$$R_{\text{SPE}}^{\text{sec},k}(N) = \pi a^2 f_{\text{SPE}} \int_{E_{\text{cut}}}^{E_{\text{max}}} \frac{4a}{3w} \frac{dE}{dx} \Big|_{E'} 4\pi j_k(E', N) dE' \quad (37)$$

where  $j_k(E', N)$  with  $k = e, p$  is the spectrum of CR electrons and protons at the column density  $N$  (see Fig. 3).

The flux of SPEs propagating through the grain (in unit of electrons per  $\text{cm}^2$  per second) can be calculated as

$$\begin{aligned} \Phi_{\text{SPE}}^{\text{sec},k}(N) &= \frac{R_{\text{sec}}^{\text{SPE}}}{4\pi a^2} \\ &= f_{\text{SPE}} \frac{4\pi a}{3w} \int_{E_{\text{cut}}}^{E_{\text{max}}} 4\pi j_k(E', N) \frac{dE}{dx} \Big|_{E'} dE' \quad (38) \end{aligned}$$

Using the attenuated spectra of CR electron and protons calculated at the gas column density  $N_{\text{H}_2}$ , (see Fig.

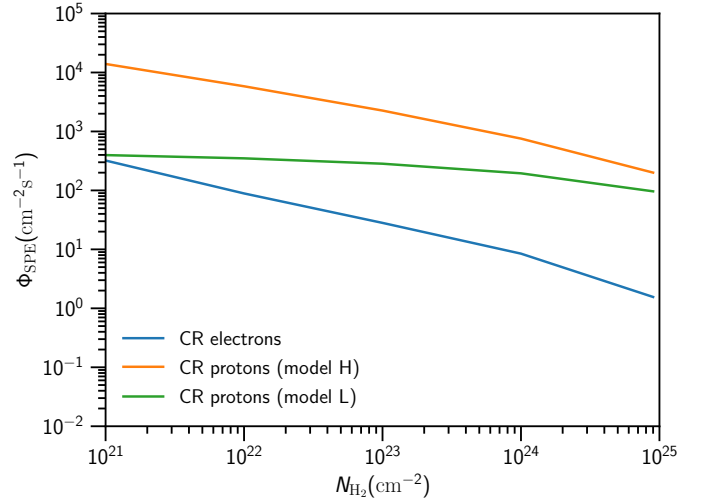


**Figure 6.** Flux of secondary SPEs emitted by CR electrons and protons bombarding silicate grains, assuming  $f_{\text{SPE}} = 0.1$ . CR protons are dominant over CR electrons in secondary electron emission.

3) and the energy loss  $dE/dx$  in Appendix B, we calculate the flux of secondary SPEs created within the silicate grain and show the results in Figure 6. The flux of SPEs by CR protons is dominant over that of CR electrons for both model H and L. For CR electrons, one sees that  $\Phi_{\text{SPE}}^{\text{sec},\text{CR}e} \approx 100, 50, 10 \text{ cm}^{-2} \text{ s}^{-1}$  at  $N_{\text{H}_2} = 10^{22}, 10^{23}, 10^{24} \text{ cm}^{-2}$ , assuming the typical value of  $f_{\text{SPE}} = 0.1$  and the grain size  $a = 1 \mu\text{m}$ . However, for CR protons (model L), one has  $\Phi_{\text{SPE}}^{\text{sec},\text{CR}p} \approx 100 \text{ cm}^{-2} \text{ s}^{-1}$  at  $N_{\text{H}_2} = 10^{22}, 10^{23}, 10^{24} \text{ cm}^{-2}$  using the same parameters.

Compared to UV flux produced by CRs obtained in Figure 5 (upper panel), the flux of secondary SPEs (Fig. 6) is generally lower. However, the reaction cross-section of electrons with molecules is larger than photons (Arumainayagam et al. 2010) (see Wu et al. (2024) for more discussion). Therefore, secondary electrons and SPEs would be important for chiral chemistry in the ice mantle.

## 6. DISCUSSION

### 6.1. *Effects of CRs on production of low-energy SPEs from Aligned Grains*

In Paper I (Hoang 2023), we first studied the origins and effect of spin-polarized electrons on chiral symmetry breaking. We suggested that dust grains aligned with the ambient magnetic fields are a ubiquitous source of spin-polarized electrons (SPEs) due to photoelectric effect caused by interstellar UV radiation. We also suggest that magnetically aligned grains could play an important role in chiral symmetry breaking of prebiotic molecules (amino acids and sugars) due to chiral-dependence adsorption of chiral molecules onto aligned grains.

Here, we have studied the effects of CRs on emission of SPEs from aligned dust grains in dense protostellar environments where interstellar UV radiation is significantly reduced. Using the popular CSDA model of CR transport, we calculate the spectra of CRs for different gas column densities and the flux of CR-induced UV radiation. We found that thermal electrons produced by CR ionization that have random spins captured to aligned grains become spin-polarized due to the Barnett effect because the timescale of the spin alignment is shorter than the electron collision time (see Section 4). Using the flux of CR-induced UV radiation, we calculate the rate of photoemission and found that CR-induced UV is dominant in producing photoelectrons from the aligned grains, including spin-polarized electrons (SPEs) (see Figures 5). CR electrons and protons can also create secondary SPEs within the silicate core of the icy grain (see Figure 6).

We note that the depolarization of SPEs is negligible for low-energy regime as shown in Hoang (2023), so SPEs can maintain their spin orientation during the passage through the grain and in the gas.

### 6.2. *Role of low-energy electrons in the formation of amino acids in ice mantles*

As shown in this paper, CRs are the dominant source of ionizing molecular gas,  $H_2$ , producing low-energy electrons in protostellar environments. Moreover, CR bombardment can also produce secondary low-energy electrons, although its flux is lower.

Experiments have demonstrated that low-energy electrons play a vital role in surface chemistry. For instance, irradiation of low-energy electrons onto the ice mantles analogous to interstellar ice was found to trigger chemical reactions in similar ways as irradiation of UV photons Boamah et al. (2014); Boyer et al. (2016); Sullivan et al. (2016); Kipfer et al. (2024). In particular, the experiment by Esmaili et al. (2018) showed that glycine

can be formed by irradiation of low-energy electrons on interstellar analog of  $CO_2$ - $CH_4$ - $NH_3$  ice (see Arumainayagam et al. 2019 for a review). Recently, Wu et al. (2024) calculated the flux of secondary electrons by CR protons and suggest that due to their larger cross-section than UV photons, secondary low-energy electrons play a more important role in ice chemistry than UV photons.

### 6.3. *Can low-energy spin-polarized electrons induce the chiral asymmetry of amino acids formed in the ice mantle?*

The role of low-energy electrons on ice chemistry is well established. Yet, to date, the effect of spin of low-energy electrons on the chirality of prebiotic molecules formed in interstellar ice analogs is not yet studied. It is well established from experiments that the chiral asymmetry of amino acids could be achieved by irradiation of UVCPL (e.g., Modica et al. 2014). Based on the similarity between UVCPL and SPEs in terms of their induced helicity described by  $H \propto \mathbf{S} \cdot \mathbf{v}$ , we conjecture that SPEs have an effect on the chiral asymmetry of molecules formed in the ice mantle of aligned grains.

We note that secondary SPEs created within the aligned grains by CRs can travel an average distance, defined by *electron escape length*,  $l_e$ . The typical value of  $l_e$  for low-energy electrons of  $\sim 10$  eV through silicate grains is  $l_e \sim 10\text{\AA}$  (see Weingartner & Draine 2001 for more details). Therefore, they can reach the outer ice mantle and trigger chemical activities on the ice mantle. Moreover, compared to UV-CPL, which is the leading mechanism for causing chiral symmetry breaking, low-energy SPEs produced by CR particles are more abundant due to the significant attenuation of UV photons. Similarly, the cross-section of electrons is larger photons. Therefore, we predict that low-energy SPEs from CRs dominate the chiral symmetry breaking in icy grain chemistry in dense protostellar environments.

### 6.4. *A model for origins of chiral asymmetry of amino acids in protostellar environments*

Icy grain mantles play an essential role in the formation of COMs, amino acids (see review by Herbst & van Dishoeck 2009), and sugars (Meinert et al. 2016). Here, following Paper I, we suggest that icy magnetic grains aligned with the ambient magnetic field in protostellar systems could be a key agent for the symmetry breaking of chiral prebiotic molecules. The scenario is illustrated in Figure 7.

First, aligned grains produce low-energy SPEs due to the photoelectric effect caused by interstellar UV photons (Hoang 2023) and CR-induced UV radiation. Sec-

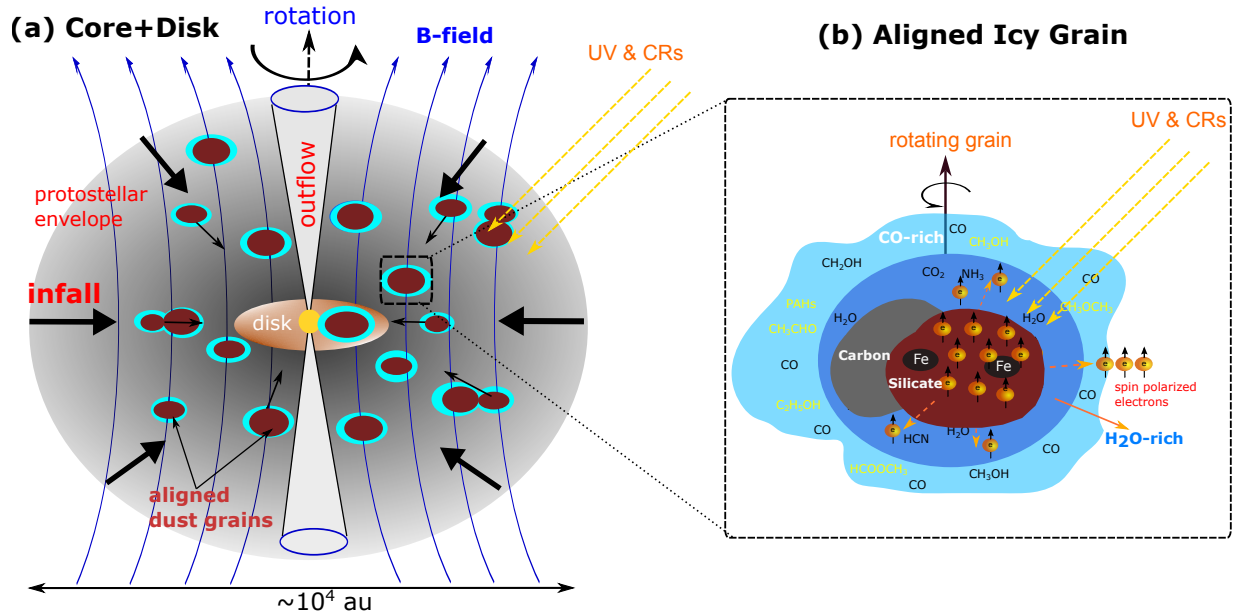


**Figure 7.** (a) Illustration of a protostellar system including envelope and the disk. Icy dust grains are aligned with magnetic fields. (b) Zoom-in a single icy grain. SPEs produced by CRs and CR-induced UV radiation impact chemical reactions and the formation of amino acids within the ice mantles. Irradiation of SPEs on molecules in the ice mantle can facilitate the formation of COMs and induce chiral asymmetry.

ondary SPEs created inside the grain by CR bombardment would travel to the ice mantle and have important effects on the chemical synthesis within the ice mantle (see Figure 1), as shown by experiments with electron irradiation on interstellar ice analogs. When accounting for the electron spin, SPEs differently interact with chiral molecules on the aligned grain ice mantle, causing the chiral asymmetry due to the dependence of reaction rates of chiral molecules on electron spins (Rosenberg et al. 2008; Rosenberg 2019; Ozturk & Sasselov 2022).

Second, aligned icy grains containing aligned electron spins could act as the magnetic surface that induces the chiral-selective adsorption of chiral molecules in the gas phase due to exchange interaction (Banerjee-Ghosh et al. 2018; Ozturk et al. 2023b), leading to the accumulation of a preferred enantiomer of chiral molecules than the other and chiral asymmetry. Finally, aligned grains can act as a chiral agent which helps form more complex molecules of similar chirality and increase chiral asymmetry thanks to magnetic dipole-dipole interaction (Hoang 2023). Finally, the resulting SPEs induced by CR-induced UV radiation will escape into the gas and interact with nearby icy grains before they are captured by hydrogen molecules, as shown in (Hoang 2023). This flow of SPEs can cause the chiral asymmetry on icy grains in planet-forming disks and cause the initial enantiomer excess.

In our proposed scenario, amino acids formed intrinsically chiral asymmetry in aligned icy grains. Ice

grains with amino acids become building blocks of planets, comets, and asteroids. Some amino acids from comets/asteroids may be delivered to Earth and act as origins of life. Amino acids in the ice mantle are racemic, but those adsorb/crystallize onto the grain core are chiral asymmetric due to the spin exchange interaction (Rosenberg et al. 2008; Tassinari et al. 2019). The advantage of this model is that chiral asymmetry is protected from further destruction due to the shield from energetic radiation/particles. In particular, our model can explain the leading explanation for the extraterrestrial origin of amino acids in carbonaceous meteorites that were formed from the ISM as demonstrated by isotopic analysis of deuterium (Engel & Macko 1997; Pizzarello & Huang 2005; Glavin et al. 2020a,b).

Note that our proposed model is different from the model by Greenberg (1996). In Greenberg’s model, amino acids are formed in the ice mantle of grains in molecular clouds. Subsequently, the clouds pass through the UV circularly polarized light from neutron stars. However, to date, no measurements of UVCPL from neutron stars are reported (see (Bailey 2001) for more discussion). Our proposed model here shares the similarity with Greenberg’s model by assuming amino acids formed in the ice mantle, but it relies on the in-situ SPE from the grain core by CR bombardment to cause the symmetry breaking of amino acids.

Finally, our proposed mechanism can be extended to other objects (e.g., planetesimals, comets, and aster-

oids) that grow from grain coagulation of aligned grains (Hoang 2022) because CRs can penetrate tens of meters within the object and create secondary SPEs. These has direct implications for the origin of life in the universe.

#### 6.5. *How to observe chiral molecules and chiral asymmetry in astrophysical environments?*

Chiral organic molecules can be detected through the vibrational transitions in the C-C and C-H bonds, which occurs in mid-IR. A more convenient technique is based on the rotational transitions of molecules in radio (rotational spectroscopy). The first chiral molecule, prolyline oxide, is detected in a shell around the massive protostar in the Sgr B2 star-forming region by McGuire et al. (2016) using rotational spectroscopy observed at 11 GHz by GBT, but the enantiomer excess of this molecule is unknown.

The unique method to detect chirality (i.e., handedness) of chiral molecules is using the circular polarization of light. Chiral molecules absorb or scatter dominantly the left-handed/right-handed CP light due to the interaction of the electric field of light with the chiral molecular (Sparks et al. 2009b,a; Patty et al. 2021; Gleiser 2022). For example, linearly polarized light will be rotated by the absorption or scattering of chiral molecules. Therefore, by observing the CP of scattered light, one can infer the chirality. Sparks et al. (2009b) detected CP of light scattered by photosynthetic microbes. Lankhaar (2022) calculated the CP signal expected from a simple amino acid detected toward the GC and found the signal is rather small. It is thus very challenging to detect such a small signal due to a small enantiomer excess of amino acids. The most viable method detecting chiral assymetry of prebiotic molecules is through in-situ measurements of dust in the Zodiacal cloud and from active commets/asteroids and direct analysis of meteorite.

## 7. SUMMARY

We studied the effects of CRs and CR-induced radiation on the production of SPEs from aligned grains in dense protostellar environments and discuss their implications for chiral symmetry breaking. Our main findings are summarized as follows:

1. Assuming the most likely composite dust model for the dense regions consisting of the Astro dust core and an ice mantle, we find that dust grains are efficiently aligned with the magnetic fields by magnet-

ically enhanced radiative torque (MRAT) mechanism in dense protostellar environments. Electron spins are aligned within such magnetically aligned grains with the ambient magnetic field.

2. We find that thermal electrons having random spins captured by aligned grains will become spin-polarized due to the Barnett effect, converting randomly electron spins to aligned spins.
3. Using the continuous slowing down approximation model for modeling the CR transport in dense regions, we calculate the CR-induced UV radiation by H<sub>2</sub> fluorescence. We find that local UV radiation induced by induces the photoemission of spin-polarized electrons from aligned dust grains, which are the important source of SPEs in dense environments.
4. CRs can also create secondary SPEs within the grain core, which may trigger chemical reactions and help form complex molecules and amino acids in the icy mantles of the aligned grain.
5. Due to the physical similarity between UV-CPL and SPEs in terms of spins and helicity, we suggest that SPEs produced by CRs could play an important role in surface chemistry in ice mantles of grains and might produce symmetry breaking for resulting amino acids in star- and planet-forming regions.
6. We suggest a novel model for explaining the origins of amino acids detected in meteorite, comets, and asteroids, which is based the effect of SPEs induced by CRs on aligned grains and ice mantles in protostellar environments. Our proposed mechanism has advantage over UVCPL because CRs can penetrate deep into the planet-forming regions.

## ACKNOWLEDGMENTS

We thank Phan Vo Hong Minh for discussions on cosmic ray transport in molecular clouds. This work is supported by the research planning for exploring cosmic life phenomena (LiCE) project (No. 2024E84100) funded by Korea Astronomy and Space Science (KASI). This work was partly supported by a grant from the Simons Foundation to IFIRSE, ICISE (916424, N.H.). We would like to thank the ICISE staff for their enthusiastic support.

## REFERENCES

- Altwegg, K., Balsiger, H., Bar-Nun, A., et al. 2016, *Science Advances*, 2, e1600285
- Arumainayagam, C. R., Lee, H.-L., Nelson, R. B., Haines, D. R., & Gunawardane, R. P. 2010, *Surface Science Reports*, 65, 1
- Arumainayagam, C. R., Garrod, R. T., Boyer, M. C., et al. 2019, *Chemical Society Reviews*, 48, 2293
- Bailey, J. 2001, *Origins of life and evolution of the biosphere*, 31, 167
- Bailey, J., Chrysostomou, A., Hough, J. H., et al. 1998, *Science*, 281, 672
- Banerjee-Ghosh, K., Dor, O. B., Tassinari, F., et al. 2018, *Science*, 360, 1331
- Barnett, S. J. 1915, *Physical Review*, 6, 239
- Bernstein, M. P., Dworkin, J. P., Sandford, S. A., Cooper, G. W., & Allamandola, L. J. 2002, *Nature*, 416, 401
- Bialy, S., Belli, S., & Padovani, M. 2022, *A&A*, 658, L13
- Blackmond, D. G. 2004, *ChemInform*, 35, no
- Boamah, M. D., Sullivan, K. K., Shulenberg, K. E., et al. 2014, *Faraday Discussions*, 168, 249
- Bonner, W. A. 1991, *Origins of Life and Evolution of the Biosphere*, 21, 59
- Boyer, M. C., Rivas, N., Tran, A. A., Verish, C. A., & Arumainayagam, C. R. 2016, *Surface Science*, 652, 26
- Caro, G. M. M., Meierhenrich, U. J., Schutte, W. A., et al. 2002, *Nature*, 416, 403
- Caselli, P., & Ceccarelli, C. 2012, *The A&A Review*, 20, 151
- Caselli, P., Walmsley, C. M., Terzieva, R., & Herbst, E. 1998, *ApJ*, 499, 234
- Cristofari, P. 2021, *Universe*, 7, 324
- Cronin, J., & Pizzarello, S. 1997, *Science*, 81, 73
- Draine, B. T., & Salpeter, E. E. 1979, *ApJ*, 231, 77
- Elsila, J. E., Dworkin, J. P., Bernstein, M. P., Martin, M. P., & Sandford, S. A. 2007, *The Astrophysical Journal*, 660, 911
- Engel, M. H., & Macko, S. A. 1997, *Nature*, 389, 265
- Esmaili, S., Bass, A. D., Cloutier, P., Sanche, L., & Huels, M. A. 2018, *The Journal of Chemical Physics*, 148, 164702
- Fano, U. 1963, *Annual Review of Nuclear and Particle Sciences*, 13, 1
- Flores, J. J., Bonner, W. A., & Massey, G. A. 1977, *Journal of the American Chemical Society*, 99, 3622
- Gabici, S., Evoli, C., Gaggero, D., et al. 2019, *International Journal of Modern Physics D*, 28, 1930022
- Gabici, S., & Montmerle, T. 2015, in *International Cosmic Ray Conference*, Vol. 34, 34th International Cosmic Ray Conference (ICRC2015), 29
- Gaches, B. A. L., & Offner, S. S. R. 2018, *ApJ*, 861, 87
- Galametz, M., Maury, A. J., Valdivia, V., et al. 2019, *A&A*, 632, A5
- Giang, N. C., Hoang, T., Kim, J.-G., & Tram, L. N. 2023, *Monthly Notices of the Royal Astronomical Society*, 520, 3788
- Glavin, D. P., Burton, A. S., Elsila, J. E., Aponte, J. C., & Dworkin, J. P. 2020a, *Chemical Reviews*, 120, 4660
- Glavin, D. P., Elsila, J. E., Burton, A. S., et al. 2012, *Meteoritics & Planetary Science*, 47, 1347
- Glavin, D. P., McLain, H. L., Dworkin, J. P., et al. 2020b, *Meteoritics & Planetary Science*, 55, 1979
- Gleiser, M. 2022, *Origins of Life and Evolution of Biospheres*, 52, 93
- Greenberg, J. M. 1996, *AIP Conference Proceedings*, 185
- Greenberg, J. M., & Li, A. 1998, *A&A*, 332, 374
- Hegstrom, R. A., Rein, D. W., & Sandars, P. G. H. 1980, *The Journal of Chemical Physics*, 73, 2329
- Hensley, B. S., & Draine, B. T. 2021, *The Astrophysical Journal*, 906, 0
- Herbst, E., & van Dishoeck, E. F. 2009, *ARA&A*, 47, 427
- Hoang, T. 2022, *ApJ*, 928, 102
- Hoang, T. 2023, *ArXiv:2312.15934*, *ApJ*, in press
- Hoang, T., & Lazarian, A. 2008, *MNRAS*, 388, 117
- Hoang, T., & Lazarian, A. 2016a, *ApJ*, 831, 159
- Hoang, T., & Lazarian, A. 2016b, *ApJ*, 821, 91
- Hoang, T., Lazarian, A., & Schlickeiser, R. 2015, *ApJ*, 806, 255
- Hoang, T., & Loeb, A. 2017, *ApJ*, 848, 0
- Hoang, T., Tram, L. N., Lee, H., Diep, P. N., & Ngoc, N. B. 2021, *ApJ*, 908, 218
- Hoang, T., Tram, L. N., Minh Phan, V. H., et al. 2022, *AJ*, 164, 248
- Hoang, T., & Truong, B. 2024, *The Astrophysical Journal*, 965, 183
- Indriolo, N., & McCall, B. J. 2012, *ApJ*, 745, 91
- Ioppolo, S., Fedoseev, G., Chuang, K.-J., et al. 2021, *Nature Astronomy*, 5, 197
- Ivlev, A. V., Padovani, M., Galli, D., & Caselli, P. 2015, *The Astrophysical Journal*, 812, 135
- Jenkins, E. B. 2009, *ApJ*, 700, 1299
- Kipfer, K. A., Galli, A., Riedo, A., et al. 2024, *Icarus*, 410, 115742
- Kisker, E., Gudat, W., & Schröder, K. 1982, *Solid State Communications*, 44, 591
- Kvenvolden, K., Lawless, J., Pering, K., et al. 1970, *Nature*, 228, 923
- Kwon, J., Tamura, M., Hough, J. H., et al. 2016, *The Astrophysical Journal*, 824, 95
- Kwon, J., Nakagawa, T., Tamura, M., et al. 2018, *The Astronomical Journal*, 156, 0



- Kwon, W., Looney, L. W., Mundy, L. G., Chiang, H.-F., & Kembball, A. J. 2009, *ApJ*, 696, 841
- Lankhaar, B. 2022, *Astronomy & Astrophysics*, 666, A126
- Lazarian, A. 2007, *J. Quant. Spectrosc. Rad. Trans.*, 106, 225
- Lazarian, A., Andersson, B.-G., & Hoang, T. 2015, in *Polarimetry of stars and planetary systems*, ed. L. Kolokolova, J. Hough, & A.-C. Levasseur-Regourd ((New York: Cambridge Univ. Press)), 81
- Lazarian, A., & Hoang, T. 2007, *MNRAS*, 378, 910
- Lazarian, A., & Hoang, T. 2021, *ApJ*, 908, 12
- Lee, T. D., & Yang, C. N. 1956, *Physical Review*, 104, 254
- Lindhard, J., & Scharff, M. 1961, *Physical Review*, 124, 128
- Mathis, J. S., Mezger, P. G., & Panagia, N. 1983, *A&A*, 128, 212
- McGuire, B. A., Carroll, P. B., Loomis, R. A., et al. 2016, *Science*, 352, 1449
- Meinert, C., Myrgorodska, I., Marcellus, P. d., et al. 2016, *Science*, 352, 208
- Meng, F., Sánchez-Monge, Á., Schilke, P., et al. 2019, *A&A*, 630, A73
- Miller, S. L., & Urey, H. C. 1959, *Science*, 130, 245
- Miotello, A., Testi, L., Lodato, G., et al. 2014, *A&A*, 567, A32
- Modica, P., Martins, Z., Meinert, C., Zanda, B., & d'Hendecourt, L. L. S. 2018, *The Astrophysical Journal*, 865
- Modica, P., Meinert, C., Marcellus, P. d., et al. 2014, *The Astrophysical Journal*, 788, 79
- Morlino, G., Blasi, P., Peretti, E., & Cristofari, P. 2021, *MNRAS*, 504, 6096
- Naaman, R., Paltiel, Y., & Waldeck, D. H. 2018, *CHIMIA International Journal for Chemistry*, 72, 394
- Naaman, R., & Waldeck, D. H. 2012, *The Journal of Physical Chemistry Letters*, 3, 2178
- Neufeld, D. A., & Wolfire, M. G. 2017, *ApJ*, 845, 163
- Oba, Y., Takano, Y., Dworkin, J. P., & Naraoka, H. 2023, *Nature Communications*, 14, 3107
- Oba, Y., Takano, Y., Watanabe, N., & Kouchi, A. 2016, *The Astrophysical Journal Letters*, 827, L18
- Ozturk, S. F., Bhowmick, D. K., Kapon, Y., et al. 2023a, *Nature Communications*, 14, 6351
- Ozturk, S. F., Liu, Z., Sutherland, J. D., & Sasselov, D. D. 2023b, *Science Advances*, 9, eadg8274
- Ozturk, S. F., & Sasselov, D. D. 2022, *Proceedings of the National Academy of Science*, 119, e2204765119
- Padovani, M., Galli, D., & Glassgold, A. E. 2009, *Astronomy & Astrophysics*, 501, 619
- Padovani, M., Galli, D., Scarlett, L. H., et al. 2024, *Astronomy & Astrophysics*, 682, A131
- Padovani, M., Hennebelle, P., Marcowith, A., & Ferrière, K. 2015, *A&A*, 582, L13
- Padovani, M., Marcowith, A., Hennebelle, P., & Ferrière, K. 2016, *A&A*, 590, A8
- Padovani, M., Marcowith, A., Sánchez-Monge, Á., Meng, F., & Schilke, P. 2019, *A&A*, 630, A72
- Parizot, E., Marcowith, A., van der Swaluw, E., Bykov, A. M., & Tatischeff, V. 2004, *A&A*, 424, 747
- Parker, E. T., McLain, H. L., Glavin, D. P., et al. 2023, *Geochimica et Cosmochimica Acta*, 347, 42
- Patty, C. H. L., Kühn, J. G., Lambrev, P. H., et al. 2021, *Astronomy & Astrophysics*, 651, A68
- Pfandzelter, R., Winter, H., Uragil'din, I., & Rösler, M. 2003, *Physical Review B*, 68, 165415
- Phan, V. H. M., Gabici, S., Morlino, G., et al. 2020, *A&A*, 635, A40
- Phan, V. H. M., Schulze, F., Mertsch, P., Recchia, S., & Gabici, S. 2021, *PhRvL*, 127, 141101
- Pizzarello, S., & Cronin, J. R. 1998, *Nature*, 394, 236
- Pizzarello, S., & Huang, Y. 2005, *Geochimica et Cosmochimica Acta*, 69, 599
- Potyszil, C., Ota, T., Yamanaka, M., et al. 2023, *Nature Communications*, 14, 1482
- Purcell, E. M. 1979, *ApJ*, 231, 404
- Ray, K., Ananthavel, S. P., Waldeck, D. H., & Naaman, R. 1999, *Science*, 283, 814
- Redaelli, E., Sipilä, O., Padovani, M., et al. 2021, *A&A*, 656, A109
- Rivilla, V. M., Jiménez-Serra, I., Martín-Pintado, J., et al. 2022, *Frontiers in Astronomy and Space Sciences*, 9, 876870
- Rivilla, V. M., Sanz-Novato, M., Jiménez-Serra, I., et al. 2023, *The Astrophysical Journal Letters*, 953, L20
- Rosenberg, R. A. 2019, *Symmetry*, 11, 528
- Rosenberg, R. A., Haija, M. A., & Ryan, P. J. 2008, *Physical Review Letters*, 101, 178301
- Rosenberg, R. A., Mishra, D., & Naaman, R. 2015, *Angewandte Chemie International Edition*, 54, 7295
- Rudd, M. E., DuBois, R. D., Toburen, L. H., Ratcliffe, C. A., & Goffe, T. V. 1983, *Physical Review A*, 28, 3244
- Sabatini, G., Bovino, S., & Redaelli, E. 2023, *ApJL*, 947, L18
- Savage, B. D., & Bohlin, R. C. 1979, *The Astrophysical Journal*, 229, 136
- Scherer, K., Fichtner, H., Ferreira, S. E. S., Büsching, I., & Potgieter, M. S. 2008, *ApJL*, 680, L105
- Soai, K., Kawasaki, T., & Matsumoto, A. 1995, *Nature*, 14, 70
- Sorrell, W. H. 1994, *Monthly Notices of the Royal Astronomical Society*, 268, 40

- Sparks, W., Hough, J., & Kolokolova, L. 2015, in Polarimetry of Stars and Planetary Systems, ed. L. Kolokolova, J. Hough, & A.-C. Levasseur-Regourd ((New York: Cambridge Univ. Press)), 462
- Sparks, W., Hough, J., Kolokolova, L., et al. 2009a, *Journal of Quantitative Spectroscopy and Radiative Transfer*, 110, 1771
- Sparks, W. B., Hough, J., Germer, T. A., et al. 2009b, *Proceedings of the National Academy of Sciences*, 106, 7816
- Sternheimer, R. M., Berger, M. J., & Seltzer, S. M. 1984, *Atomic Data and Nuclear Data Tables*, 30, 261
- Sullivan, K. K., Boamah, M. D., Shulenberger, K. E., et al. 2016, *Monthly Notices of the Royal Astronomical Society*, 460, 664
- Takayanagi, K. 1973, *PASJ*
- Tassinari, F., Steidel, J., Paltiel, S., et al. 2019, *Chemical Science*, 10, 5246
- Unguris, J., Pierce, D. T., Galejs, A., & Celotta, R. J. 1982, *Physical Review Letters*, 49, 72
- Vaillancourt, J. E., Andersson, B.-G., Clemens, D. P., et al. 2020, *ApJ*, 905, 0
- Vaupré, S., Hily-Blant, P., Ceccarelli, C., et al. 2014, *A&A*, 568, A50
- Vieu, T., Gabici, S., Tatischeff, V., & Ravikularaman, S. 2022, *MNRAS*, 512, 1275
- Weingartner, J. C., & Draine, B. T. 2001, *ApJS*, 134, 263
- Whittet, D. C. B., Hough, J. H., Lazarian, A., & Hoang, T. 2008, *ApJ*, 674, 304
- Wu, C. S., Ambler, E., Hayward, R. W., Hoppes, D. D., & Hudson, R. P. 1957, *Physical Review*, 105, 1413
- Wu, Q. T., Anderson, H., Watkins, A. K., et al. 2024, *ACS Earth and Space Chemistry*, 8, 79
- Zhukovska, S., Gail, H.-P., & Tieloff, M. 2008, *A&A*, 479, 453
- Ziegler, J. F. 1999, *JAP*, 85, 1249

## APPENDIX

 A.  $H_2$  IONIZATION CROSS SECTION BY COSMIC RAYS

The  $H_2$  ionization cross-section by CR electrons is given by (Padovani et al. 2009):

$$\sigma_{H_2}^{\text{CRe}} = 4\pi a_0^2 Z F(t) G(t) \left( \frac{I(\text{H})}{I(\text{H}_2)} \right)^2, \quad (\text{A1})$$

where  $a_0 = \hbar^2/(m_e e^2)$  is the Bohr radius,  $I(\text{H}) = 13.598$  eV is the hydrogen ionization potential,  $t = E/I(\text{H}_2)$  with  $Z = 2$  for two electrons of a  $H_2$  molecule,

$$F(t) = \frac{1 - t^{1-n}}{n-1} - \left( \frac{2}{1+t} \right)^{n/2} \frac{1 - t^{1-n/2}}{n-2}, \quad (\text{A2})$$

$$G(t) = \frac{1}{t} \left( A_1 \ln t + A_2 + \frac{A_3}{t} \right), \quad (\text{A3})$$

where  $n = 2.4 \pm 0.2$ ,  $A_1 = 0.74 \pm 0.02$ ,  $A_2 = 0.87 \pm 0.06$ ,  $A_3 = -0.60 \pm 0.05$ .

The  $H_2$  ionization cross-section by CR protons is given by

$$\sigma_{\text{CRp}} = (\sigma_1^{-1} + \sigma_h^{-1})^{-1}, \quad (\text{A4})$$

where

$$\sigma_1 = 4\pi a_0^2 C x^D, \quad (\text{A5})$$

$$\sigma_h = 4\pi a_0^2 (A \ln(1+x) + B) x^{-1}, \quad (\text{A6})$$

where  $x = m_e E/(m_H I(\text{H}))$ , and  $A = 0.71$ ,  $B = 1.63$ ,  $C = 0.51$ ,  $D = 1.24$  (Rudd et al. 1983).

The cross-section for the electron capture of CR protons via the  $p + H_2 \rightarrow H + H_2^+$  is

$$\sigma_{\text{CRp}}^{e.c.} = 4\pi a_0^2 A Z \left( \frac{I(\text{H})}{I(\text{H}_2)} \right)^2 \frac{x^2}{(C + x^B + D x^F)}, \quad (\text{A7})$$

where  $m_e E/(m_H I(\text{H}))$ ,  $A = 1.044$ ,  $B = 2.88$ ,  $C = 0.016$ ,  $D = 0.136$ ,  $F = 5.86$  (Rudd et al. 1983).

## B. ENERGY LOSS OF CR ELECTRONS AND PROTONS

## B.1. CR protons

Consider the interaction of an incident CR ion (projectile) of charge  $Z_P e$  and kinetic energy  $E$  (velocity  $\beta c$ ) with an electron of the target atom. Let  $Z_{T,i}$  be the atomic number of target element  $i$ . The total energy loss of the incident ion per pathlength, which is usually referred to as *stopping power* of the material, is given by

$$\frac{dE_{\text{ion}}}{dx} = \sum_i n_i S_i, \quad (\text{B8})$$

where  $n_i$  is the atomic number density of element  $i$  in the gas or dust,  $S_i$  is the electronic stopping cross-section of element  $i$  in units of eV cm<sup>2</sup>, and the sum is taken over all elements  $i$  present in the grain. For the  $H_2$  gas,  $n_i = n_{H_2}$ . For the silicate grains of structure  $\text{MgFeSiO}_4$ , the summation is over all these elements with their respective fraction.

The Bethe-Bloch theory yields the following (see Fano 1963):

$$S_i = \frac{4\pi (Z_P e^2)^2}{m_e c^2 \beta^2} Z_{T,i} \left[ \frac{1}{2} \ln \frac{2\gamma^2 m_e c^2 \beta^2 T_{\text{max}}}{I_i^2} - \beta^2 - \frac{C}{Z_{T,i}} - \frac{\delta}{2} \right], \quad (\text{B9})$$

where  $T_{\text{max}}$  is the maximum energy transferred from the ion to the atomic electron, and  $I_i$  is the mean excitation energy of element  $i$ . Here  $C/Z_{T,i}$  is the shell correction term, and  $\delta/2$  is the density correction term.

In binary collisions,  $T_{\max}$  is given by

$$T_{\max} = \frac{2\gamma^2 M_P^2 m_e c^2 \beta^2}{m_e^2 + M_P^2 + 2\gamma m_e M_P}, \quad (\text{B10})$$

where  $M_P$  is the atomic mass of the projectile.

In the case  $2\gamma m_e/M_P \ll 1$  (heavy ion or not very high  $\gamma$ ) we have  $T_{\max} = 2\gamma^2 \beta^2 m_e c^2$ . Thus Equation (??) can be rewritten as

$$S_i = \frac{4\pi(Z_P e^2)^2}{m_e c^2 \beta^2} Z_{T,i} \left[ \ln \frac{2m_e c^2 \beta^2}{I_i} + \mathcal{L}(\beta) \right], \quad (\text{B11})$$

where

$$\mathcal{L}(\beta) = \ln \frac{1}{1 - \beta^2} - \beta^2 - \frac{C}{Z_{T,i}} - \frac{\delta}{2}. \quad (\text{B12})$$

where the shell correction term  $C/Z_{T,i}$  is maximum at  $\sim 0.3$  and becomes negligible for  $E > 10$  MeV/amu. The density correction term  $\delta/2$  is important and increases to above 1 for  $E > 5$  GeV/amu (see Ziegler 1999 for more details). Here we calculate  $\delta/2$  using an analytical fit from Sternheimer et al. (1984).

For energy below 1 MeV, the energy loss is given by (Lindhard & Scharff 1961)

$$S_i = 8\pi e^2 a_0 Z_P^{1/6} \frac{Z_P Z_T}{Z} \frac{\beta c}{v_{\text{Bohr}}} \quad (\text{B13})$$

where

$$Z = \left( Z_P^{2/3} + Z_T^{2/3} \right)^{3/2} \quad (\text{B14})$$

and  $v_{\text{Bohr}} = e^2/\hbar$ .

## B.2. CR electrons

The energy loss of a CR electron with kinetic energy  $E$  per pathlength in the dust grain due to electronic excitations is equal to (see Hoang et al. 2015)

$$\frac{dE_{\text{el}}}{dx} = \sum_i n_i S_{\text{el},i}, \quad (\text{B15})$$

$$(\text{B16})$$

where  $S_{\text{el},i}$  is the energy loss (or stopping power) caused by atom  $i$  of charge number  $Z_{T,i}$  given by

$$S_{\text{el},i} = \frac{4\pi e^4}{m_e c^2 \beta^2} Z_{T,i} \left[ \frac{1}{2} \ln \left( \frac{E^2 \gamma + 1}{I_i^2} \right) + \frac{\mathcal{F}(\gamma)}{2} \right], \quad (\text{B17})$$

where

$$\mathcal{F}(\gamma) = - \left( \frac{2}{\gamma} - \frac{1}{\gamma^2} \right) \ln 2 + \frac{1}{\gamma^2} + \frac{1}{8} \left( 1 - \frac{1}{\gamma} \right)^2. \quad (\text{B18})$$

## C. CONTINUOUS SLOWING DOWN APPROXIMATION (CSDA) MODEL FOR CR TRANSPORT IN PROTOSTELLAR CORES

When penetrating the protostellar core, CRs lose energy due to interaction with  $H_2$ . The CR energy loss is described by the loss function

$$L(E) = \frac{1}{n_{H_2}} \frac{dE}{dx}, \quad (\text{C19})$$

where  $n_{H_2}$  is the  $H_2$  density of the gas.

Following the CSDA model of CR transport (Takayanagi 1973), the flux of CR particles is conserved such that

$$j_k(E)dE = j_k(E_0)dE_0. \quad (\text{C20})$$

The decrease in the energy of CRs after a pathlength  $dx$  is given by

$$dE = L_k(E)n_{\text{H}_2}dx = L_k(E)dN, \quad (\text{C21})$$

where  $dN = n_{\text{H}_2}dx$ , which implies

$$\frac{dE_0}{dE} = \frac{L_k(E_0)}{L_k(E)}. \quad (\text{C22})$$

From the above equations, one can obtain

$$j_k(E) = j_k(E_0) \frac{L_k(E_0)}{L_k(E)}, \quad (\text{C23})$$

which links the original flux and the final flux.

The total column density required to decrease from  $E_0$  to  $E$  is given by

$$N_{\text{H}_2} = \int_0^{N_{\text{H}_2}} dN = \int_{E_0}^E \frac{dE'}{L_k(E')} = n_{\text{H}_2} [R(E_0) - R(E)], \quad (\text{C24})$$

where the range  $dR = \frac{dE'}{n_{\text{H}_2}L_k(E')}$ .

For a given  $N_{\text{H}_2}$ , the above equation links the original energy and the final energy  $E$ . To get the exact relationship, we calculate  $N_{\text{H}_2}$  for a grid of  $E_0$  and  $E$ . Then, we select a contour level  $N_{\text{H}_2}$  and infer the parameters  $E, E_0$  which is then fitted by an analytical function

$$E_0 = \left( cE^b + \frac{N_{\text{H}_2}}{N_0} \right)^{1/b}, \quad (\text{C25})$$

where  $b, c, N_0$  are the fitting parameters.

To calculate the CR spectrum at a specific column density,  $j_k(E, N_{\text{H}_2})$ , we use Eq. C23 where  $E_0$  is given by Eq.C25.

Figure 8 shows the contour map of  $N_{\text{H}_2}$  for CR electrons. For each contour of a given  $N_{\text{H}_2}$ , one can obtain a relationship between the original energy  $E_0$  to the energy  $E$  of the CR particle that already traverses the column  $N_{\text{H}_2}$ .

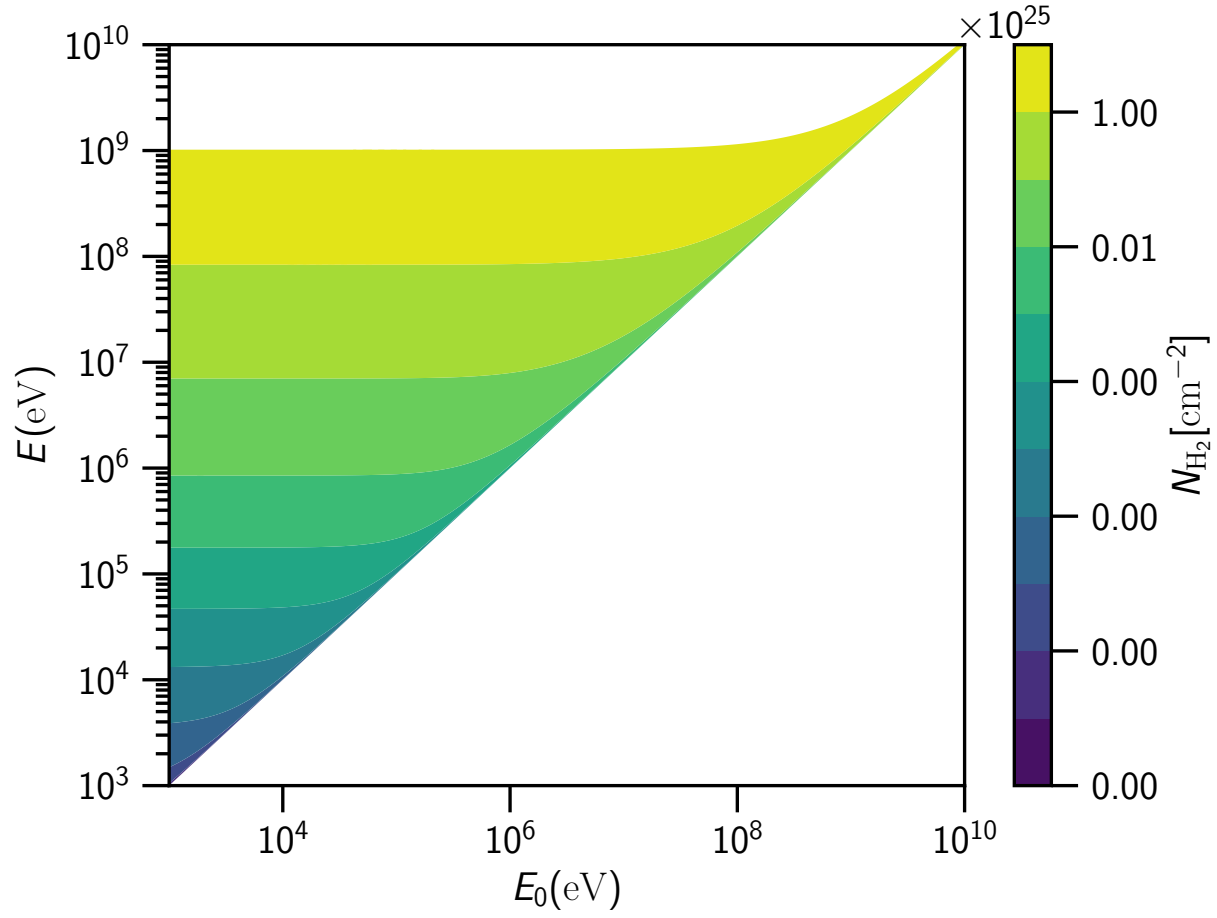


**Figure 8.** Contours of  $N_{\text{H}_2}$  as functions of  $E_0$  and  $E$  for energy loss of CR electrons in the  $\text{H}_2$  gas. For a fixed contour level  $N_{\text{H}_2}$ , there is a unique relationship between the energy of CRs after passing through that column density,  $E$ , to the initial energy of CRs  $E_0$ .